Soil Dynamics and Earthquake Engineering 191 (2025) 109264

Contents lists available at ScienceDirect

Soil Dynamics and Earthquake Engineering

journal homepage: www.elsevier.com/locate/soildyn

Nonlinear stiffened inertial amplifier tuned mass friction dampers

Sudip Chowdhury *, Sondipon Adhikari

Glasgow Computational Engineering Centre, James Watt School of Engineering, The University of Glasgow, Glasgow, Scotland, United Kingdom

ARTICLE INFO

Keywords:
Nonlinear stiffened inertial amplifier tuned mass friction damper
Nonlinear compound stiffened inertial amplifier tuned mass friction dampers
Nonlinear nested stiffened inertial amplifier tuned mass friction dampers
And nonlinear levered stiffened inertial amplifier tuned mass friction dampers
H_2 and H∞ optimisation strategies

ABSTRACT

The nonlinear stiffened inertial amplifier tuned mass friction damper (NSIATMFD) is introduced in this paper to address the limitations of the conventional tuned mass dampers such as narrow frequency ranges and limited adaptability. In addition, three more novel dampers, such as nonlinear compound stiffened inertial amplifier tuned mass friction dampers (NCSIATMFD), nonlinear nested stiffened inertial amplifier tuned mass friction dampers (NNSIATMFD), and nonlinear levered stiffened inertial amplifier tuned mass friction dampers (NLSIATMFD), are introduced by integrating stiffness and mass amplification mechanisms to increase their vibration reduction capacities. These novel dampers are applied at the top of structures to control their dynamic responses. Newton's second law is followed to derive the governing equations of motion of the controlled structures. H_2 and H_∞ optimisation strategies are utilised to derive the exact closed-form expressions for the optimal design parameters of these dampers. The transfer function is developed to derive the frequency domain responses by considering harmonic and random excitations. The frequency domain responses are further validated through numerical studies conducted using the Newmark-beta method and near-field earthquake records. Compared to the conventional tuned mass dampers (TMD), the proposed dampers achieve vibration reduction improvements of 24.24 %, 24.64 %, 23.92 %, and 24.54 %, respectively. The integration of stiffness elements significantly extends the frequency control range, while the frictional damping element enhances energy dissipation capabilities. These results establish the novel designs as effective solutions for dynamic environments, offering robust and adaptive vibration mitigation for structures exposed to diverse excitations, including seismic loads. This research provides a significant advancement in TMD technology for modern engineering applications.

1. Introduction

Vibration mitigation is an essential component of modern engineering, applicable to civil structures [1], mechanical systems, and precision equipment [2]. Tuned Mass Dampers (TMDs) are extensively used to mitigate mechanical vibrations via the application of resonance and damping principles [3]. A TMD generally comprises a mass, spring, and damper arranged to resonate out of phase with the main structure, thereby dissipating vibrational energy [4]. These systems have been effectively used in buildings such as Taipei 101, bridges, and precision instruments to mitigate vibrations induced by winds, earthquakes, and operating stresses [5]. Nonetheless, despite their effectiveness, traditional TMDs face several limitations, including a narrow frequency bandwidth, challenges in adapting to varying dynamic loads, and difficulties in enhancing vibration mitigation capacity due to the increased static mass of individual dampers or the cumulative weight of an array of dampers [6].

Advances in TMD design focus on addressing these limitations by incorporating innovative mechanisms and optimisation strategies. For instance, H_2 optimisation is utilised to determine the optimal tuning frequency and damping ratios of TMDs [7] based on the mean-square dynamic responses under random excitations [8]. Similarly, H_∞ optimisation is employed to derive these parameters from the dynamic responses [9] of TMD-controlled structures subjected to harmonic excitations [10]. While these optimisation techniques enhance TMD performance, challenges related to spatial constraints and weight remain unresolved.

Inertial amplifiers offer a promising solution to these challenges by leveraging mechanical leverage and resonance to amplify inertial forces, thereby enhancing vibration isolation [11]. Conventional inertial amplifiers are designed to increase the effective mass of a system without a proportional increase in static mass [12]. These devices typically utilise geometric configurations, such as rhombus-shaped four-bar linkages, to amplify inertial forces acting on the system [13]. In particular, inertial amplifier-tuned mass dampers (IA-TMDs) specialise in mass amplification without significantly affecting stiffness [14]. This amplification is achieved through mechanisms like vertical spring-mass

---

* Corresponding author.
E-mail address: Sudip.Chowdhury@glasgow.ac.uk (S. Chowdhury).

https://doi.org/10.1016/j.soildyn.2025.109264
Received 12 November 2024; Received in revised form 5 January 2025; Accepted 24 January 2025

systems, which enhance the system's dynamic mass response [15]. However, IA-TMDs are limited to positive dynamic mass amplification, making them effective within specific frequency ranges [16]. Their inability to influence the system's stiffness restricts their applicability to broader frequency control or variable excitation conditions [17]. As a result, their vibration mitigation capacity is best suited for predictable dynamic systems where mass amplification alone suffices [18]. Therefore, a new type of IA-TMDs needs to be developed with significant effective stiffness amplification mechanisms [19]. In addition, the effective damping of the IA-TMDs needs to be enhanced significantly [20]. Therefore, a research gap has been identified.

To address the research gap, the nonlinear stiffened inertial amplifier tuned mass friction dampers (NSIATMFD) are introduced in this paper. These novel dampers incorporate both mass and stiffness amplification mechanisms. By adding stiffness components, they provide significant control over dynamic stiffness. In addition, a frictional element (i.e., Coulomb-friction characteristics) is induced inside the core of the NSIATMFDs to provide significant effective damping amplification. These novel dampers significantly outperform conventional IA-TMDs in terms of frequency control, energy dissipation, and dynamic response reduction, making them suitable for complex dynamic environments such as seismic applications or structures exposed to broadband excitations. The integration of stiffness elements into the amplifier design is the key innovation that differentiates NSIA-TMDs from their conventional counterparts. In addition, three novel dampers, such as nonlinear compound stiffened inertial amplifier tuned mass friction dampers (NCSIATMFD), nonlinear nested stiffened inertial amplifier tuned mass friction dampers (NNSIATMFD), and nonlinear levered stiffened inertial amplifier tuned mass friction dampers (NLSIATMFD), are introduced along with the NSIATMFDs to provide more advance design for overcoming most of the significant drawbacks of the conventional dampers. The equations of motion are derived by following Newton's second law. Advanced optimisation methods, such as H_2 and H_∞ optimisation schemes are applied to achieve precise system parameter tuning, ensuring robust performance under diverse conditions. The transfer matrix function is developed using Laplace transformation to obtain dynamic responses in the frequency domain. Further, the frequency domain results are validated through numerical study, considering the Newmark-beta method. The harmonic, random-white noise (Clough–Penzien power spectrum), and Northridge earthquake (near-field with pulses) are considered as loading functions. The vibration reduction capacity of the novel damper is compared with the vibration reduction capacity of the conventional dampers to find their superior vibration reduction capacities.

2. Structural models and equations of motion

Four structures with the same system parameters are considered. The structures are conceptualised as single degree of freedom (SDOF) systems. The novel dampers such as NSIATMFD, NCSIATMFD, NNSIATMFD, and NLSIATMFD are mounted at the top of the structures. Each controlled structure is conceptualised as a two-degree-of-freedom system and is shown in Fig. 1(a), Fig. 1(b), Fig. 1(c), and Fig. 1(d). ϕ defines the amplifier's angle in NSIATMFD configuration. In NCSIATMFD, ϕ and θ define primary and secondary amplifier angles. ϕ_1, ϕ_2, ϕ_3 define the primary, secondary, and tertiary amplifier angles in NNSIATMFD. The length ratios $\left(b_1/a_1\right)\left(b_2/a_2\right)$ are considered from NLSIATMFD configuration. Newton's second law has been applied to derive the governing equations of motion of the controlled SDOF systems subjected to base excitation and expressed as

$$\begin{aligned} &m_s\ddot{v}_s + c_s\dot{v}_s + k_s v_s - \beta m_e g\,\mathrm{sgn}\left(\dot{v}_d\right) - c_e\dot{v}_d - k_e v_d = -m_s\ddot{v}_g,\\ &m_e\ddot{v}_d + m_e\ddot{v}_s + \beta m_e g\,\mathrm{sgn}\left(\dot{v}_d\right) + c_e\dot{v}_d + k_e v_d = -m_e\ddot{v}_g. \end{aligned} \tag{1}$$

$v_d = u_d - u_s$ and $v_s = u_s - v_g$ define the relative deflections of each damper and SDOF system. $(\dot{\bullet})$ defines the time derivatives. m_s, $c_s = 2m_s\xi_s\omega_s$, and $k_s = m_s\omega_s^2$ define the mass, damping, and stiffness of the main structures. m_e, $c_e = 2m_e\xi_d\omega_d$, and k_e define the effective mass, damping, and stiffness of the novel damper. The exact closed-form expressions for each damper's effective mass and stiffness are listed in Table 1. β defines the friction coefficient. g defines the acceleration of gravity.

Table 1
The exact closed-form expressions for effective mass and stiffness of novel dampers.

damper	Effective mass (m_e)	Effective stiffness (k_e)
NSIATMFD	$\left(m_d + \frac{m_a}{2}(1+\cot^2\phi)\right)$	$\left(k_d + k_a\cot^2\phi\right)$
NCSIATMFD	$\left(m_d + \frac{m_a}{8}\cot^2\phi\left(1+\tan^2\theta\right)\right)$	$\left(k_d + k_a\cot^2\phi\frac{\tan^2\theta}{4}\right)$
NNSIATMFD	$\left(m_d + \frac{m_a}{2}\left(1+\cot^2\phi_3\right)\cot^2\phi_1\tan^2\phi_2\right)$	$\left(k_d + k_a\cot^2\phi_1\left(\tan^2\phi_2\cot^2\phi_3\right)\right)$
NLSIATMFD	$\left(m_d + m_a\left(\frac{b_1}{a_1}\frac{b_2}{a_2}\right)^2\right)$	$\left(k_d + k_a\left(\frac{b_1}{a_1}\frac{b_2}{a_2}\right)^2\right)$

m_d and k_d define the static mass and stiffness of the damper. m_a and k_a define the amplifier's mass and stiffness. The statistical linearisation method [8] is applied to linearise each nonlinear element of Eq. (1) and expressed as

$$c_{eq} = E\left\{\frac{\partial\left(\beta m_e g\,\mathrm{sgn}(\dot{v}_d)\right)}{\partial\dot{v}_d}\right\} = \sqrt{\frac{2}{\pi}}\frac{\beta m_e g}{\sigma_{\dot{v}_d}}. \tag{2}$$

$\sigma_{\dot{v}_d}$ defines the root mean square velocity of the damper. An error may arise during the transition of the linearised term from the nonlinear damping factor via the statistical linearisation approach which is quantified as

$$\epsilon_1 = \beta m_e g\,\mathrm{sgn}(\dot{v}_d) - \underbrace{\sqrt{\frac{2}{\pi}}\frac{\beta m_e g}{\sigma_{\dot{v}_d}}}_{c_{eq}}\dot{v}_d \tag{3}$$

where c_{eq} defines the equivalent damping of the damper.

$$\frac{\partial\epsilon_1^2}{\partial c_{eq}} = E\left\{\left(\beta m_e g\,\mathrm{sgn}(\dot{v}_d) - c_{eq}\dot{v}_d\right)^2\right\} = 0 \tag{4}$$

Therefore, no errors have been identified throughout the statistical linearisation procedure. Eq. (2) is substituted in Eq. (1) and the governing equations of motion of the controlled SDOF system have been written as

$$\begin{aligned} &m_s\ddot{v}_s + c_s\dot{v}_s + k_s v_s - \underbrace{\left(c_{eq} + c_e\right)}_{c_f}\dot{v}_d - k_e v_d = -m_s\ddot{v}_g,\\ &m_e\ddot{v}_d + m_e\ddot{v}_s + \underbrace{\left(c_{eq} + c_e\right)}_{c_f}\dot{v}_d + k_e v_d = -m_e\ddot{v}_g. \end{aligned} \tag{5}$$

The non-dimensional form of each element in Table 1 has been listed in Table 2.

The steady-state solutions for Eq. (5) have been considered as $v_s = V_s e^{\mathrm{i}\omega t}$, $v_d = V_d e^{\mathrm{i}\omega t}$, and $\ddot{v}_g = V_g e^{\mathrm{i}\omega t}$. Accordingly, the transfer matrix has been derived as

$$\begin{aligned} &\begin{bmatrix} 2q\xi_s\omega_s + q^2 + \omega_s^2 & A_{12} \\ \gamma_d\left(\mu\gamma_m + 1\right)q^2 & A_{22} \end{bmatrix} \begin{Bmatrix} V_s \\ V_d \end{Bmatrix} = -\begin{bmatrix} 1 \\ \gamma_d\left(\mu\gamma_m + 1\right) \end{bmatrix} V_g,\\ &A_{12} = -2\gamma_d\left(\mu\gamma_m + 1\right)\xi_d\omega_d q - \gamma_d\omega_d^2\left(\kappa\gamma_k + 1\right),\\ &A_{22} = \gamma_d\left(\mu\gamma_m + 1\right)q^2 + 2\gamma_d\left(\mu\gamma_m + 1\right)\xi_d\omega_d q + \gamma_d\omega_d^2\left(\kappa\gamma_k + 1\right). \end{aligned} \tag{6}$$

The transfer function for the displacement of the SDOF system has been derived as

$$\begin{aligned} X_s(q)\,|_{q=\mathrm{i}\omega} &= \frac{V_s}{V_g}\\ &= \frac{\begin{matrix} -2\mu^2 q\xi_d\gamma_d\gamma_m^2\omega_d - \kappa\mu\gamma_d\gamma_k\gamma_m\omega_d^2 - 4\mu q\xi_d\gamma_d\gamma_m\omega_d - \kappa\gamma_d\gamma_k\omega_d^2 \\ -2\mu q\xi_d\gamma_m\omega_d - \mu\gamma_d\gamma_m\omega_d^2 - \kappa\gamma_k\omega_d^2 - \mu\,q^2\gamma_m - 2q\xi_d\gamma_d\omega_d \\ -2q\xi_d\omega_d - \gamma_d\omega_d^2 - q^2 - \omega_d^2 \end{matrix}}{\Delta_e}. \end{aligned} \tag{7}$$

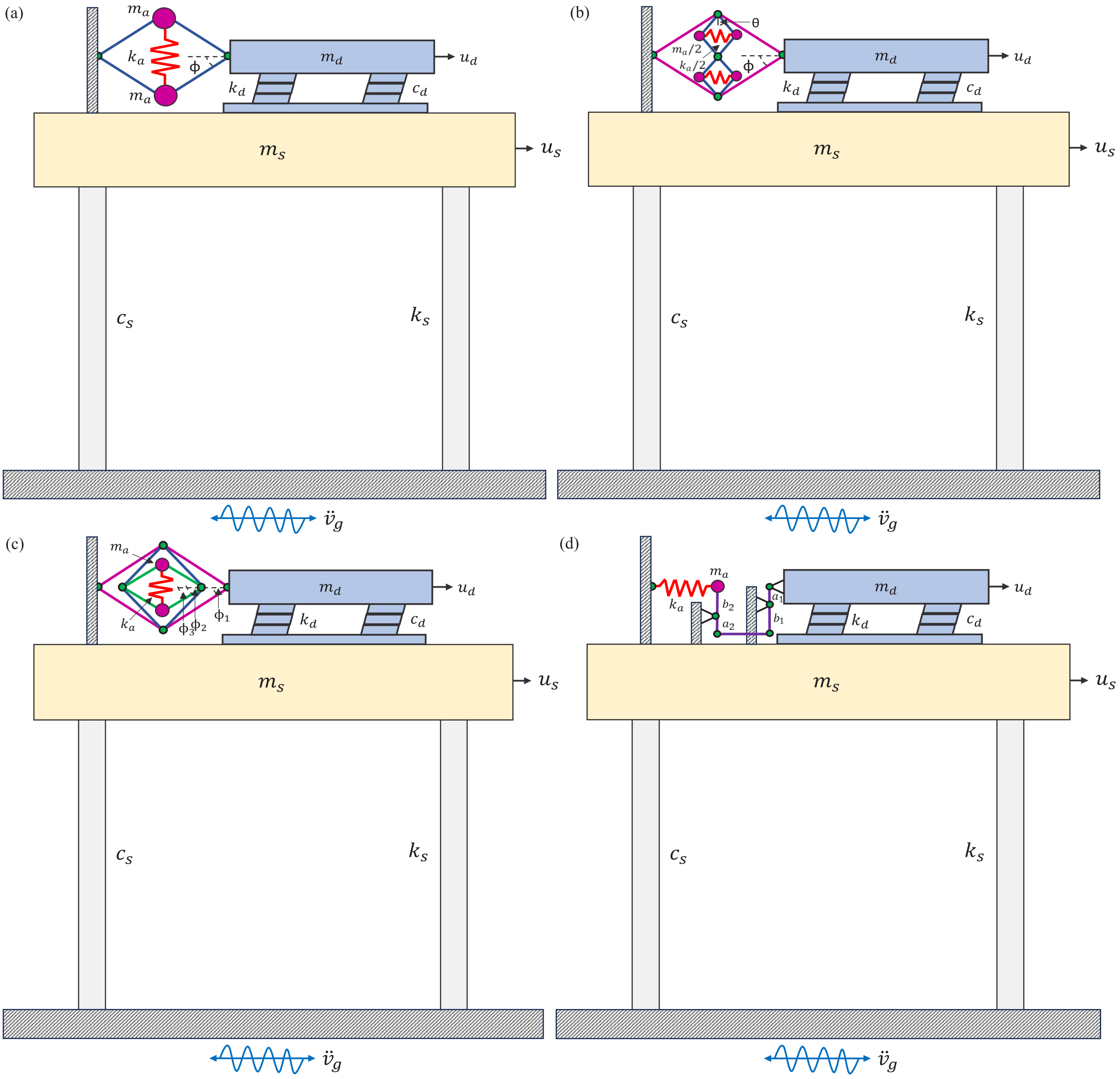

Fig. 1. The structures are controlled by (a) NSIATMFD, (b) NCSIATMFD, (c) NNSIATMFD, and (d) NLSIATMFD subjected to base excitation.

The transfer function for the displacement of the damper has been derived as

$$X_d\left(q\right)|_{q=\mathrm{i}\omega} = \frac{V_d}{V_g} = \frac{-\omega_s\left(2q\xi_s+\omega_s\right)\left(\mu\gamma_m+1\right)}{\Delta_e}. \tag{8}$$

The denominator of Eq. (7) and Eq. (8) has been derived as

$$\Delta_e = \begin{array}{c} \left(\mu\gamma_m+1\right)q^4 \\ +\left(\begin{array}{c} 2\mu^2\xi_d\gamma_d\gamma_m^2\omega_d+4\mu\xi_d\gamma_d\gamma_m\omega_d+2\mu\xi_d\gamma_m\omega_d+2\mu\xi_s\gamma_m\omega_s \\ +2\xi_d\gamma_d\omega_d+2\xi_d\omega_d+2\omega_s\xi_s \end{array}\right)q^3 \\ +\left(\begin{array}{c} \kappa\mu\gamma_d\gamma_k\gamma_m\omega_d^2+4\mu\xi_d\xi_s\gamma_m\omega_d\omega_s+\kappa\gamma_d\gamma_k\omega_d^2+\mu\gamma_d\gamma_m\omega_d^2 \\ +\kappa\gamma_k\omega_d^2+\mu\gamma_m\omega_s^2+4\xi_d\xi_s\omega_d\omega_s+\gamma_d\omega_d^2+\omega_d^2+\omega_s^2 \end{array}\right)q^2 \\ +\left(2\kappa\xi_s\gamma_k\omega_d^2\omega_s+2\mu\xi_d\gamma_m\omega_d\omega_s^2+2\xi_d\omega_d\omega_s^2+2\xi_s\omega_d^2\omega_s\right)q \\ +\kappa\gamma_k\omega_d^2\omega_s^2+\omega_d^2\omega_s^2 \end{array}. \tag{9}$$

The symbols V_s, V_d, and V_g represent the Laplace transforms of v_s, v_d, and $\ddot{v}_g$, respectively [21]. $q = \mathrm{i}\omega$, where $\mathrm{i} = \sqrt{-1}$ defines the imaginary number and ω defines the excitation frequency. Eq. (7) and Eq. (9) are further utilised to derive the standard deviation of the dynamic response of the main structure.

2.1. H_2 optimisation

Considering a white-noise random excitation, the H_2 optimisation scheme is employed to derive the optimal frequency and damping ratios of the novel dampers in terms of closed-form expressions from that standard deviation of the structure. The damping ratio of the main structure is considered zero ($\xi_s = 0$) when applying the H_2 optimisation scheme because this assumption simplifies the mathematical derivations and allows for closed-form analytical expressions for the optimal tuning frequency and damping ratio of the dampers. By neglecting the damping of the main structure, the focus shifts entirely to optimising the performance of the damper itself, eliminating interference from the structural damping effects. This approach isolates the contributions of the damper to the overall vibration control and ensures that the derived optimisation parameters are precise and effective. Therefore, $\xi_s = 0$ is substituted in Eq. (7) and Eq. (9). Accordingly, the dynamic response

Table 2
The non-dimensional form of effective mass and stiffness of novel dampers.

Damper	Effective mass ratio ($\gamma_e = m_e/m_s$)	Effective stiffness (k_e/m_s)
NSI-ATMFD	$\gamma_d\left(1+\gamma_m\underbrace{(1+\cot^2\phi)/2}_{\mu}\right)$	$\gamma_d\omega_d^2\left(1+\gamma_k\underbrace{\cot^2\phi}_{\kappa}\right)$
NCSI-ATMFD	$\gamma_d\left(1+\gamma_m\underbrace{\left(\cot^2\phi\left(1+\tan^2\theta\right)\right)/8}_{\mu}\right)$	$\gamma_d\omega_d^2\left(1+\gamma_k\underbrace{\cot^2\phi\frac{\tan^2\theta}{4}}_{\kappa}\right)$
NNSI-ATMFD	$\gamma_d\left(1+\gamma_m\underbrace{\left(1+\cot^2\phi_3\right)\cot^2\phi_1\tan^2\phi_2/2}_{\mu}\right)$	$\gamma_d\omega_d^2\left(1+\gamma_k\underbrace{\cot^2\phi_1\left(\tan^2\phi_2\cot^2\phi_3\right)}_{\kappa}\right)$
NLSI-ATMFD	$\gamma_d\left(1+\gamma_m\underbrace{\left(\frac{b_1}{a_1}\frac{b_2}{a_2}\right)^2}_{\mu}\right)$	$\gamma_d\omega_d^2\left(1+\gamma_k\underbrace{\left(\frac{b_1}{a_1}\frac{b_2}{a_2}\right)^2}_{\kappa}\right)$

$\gamma_d = m_d/m_s$ defines the mass ratio of the damper to the SDOF system.
$\gamma_m = m_a/m_d$ defines the mass ratio of amplifier to the damper.
γ_m has also been represented as $\gamma_m = \gamma_a/\gamma_d$.
$\gamma_a = m_a/m_s$ defines the mass ratio of amplifier to the SDOF system.
$\gamma_k = k_a/k_d$ defines the stiffness ratio of amplifier stiffness to the damper.
μ = Mass amplification factor of the dampers.
κ = Stiffness amplification factor of the dampers.

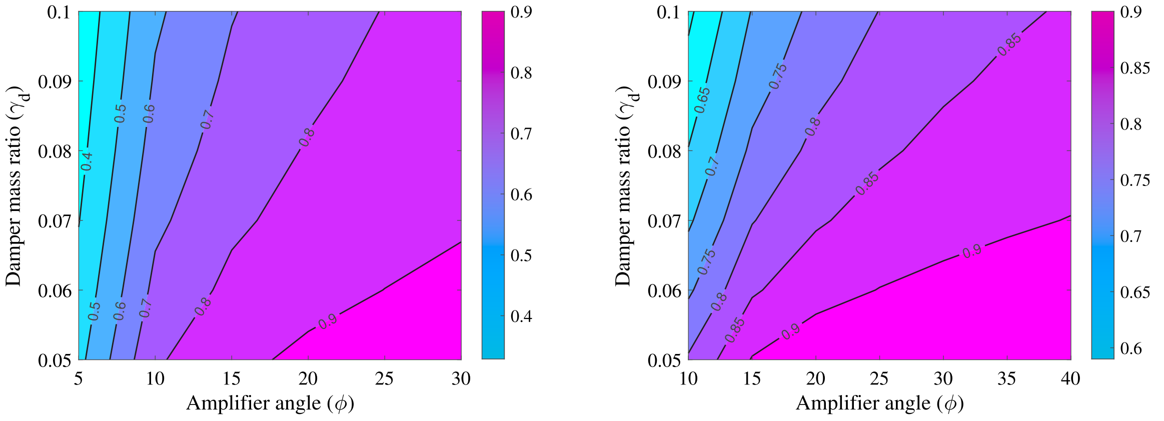

(a) NSIATMFD (b) NCSIATMFD: $\theta = 64°$

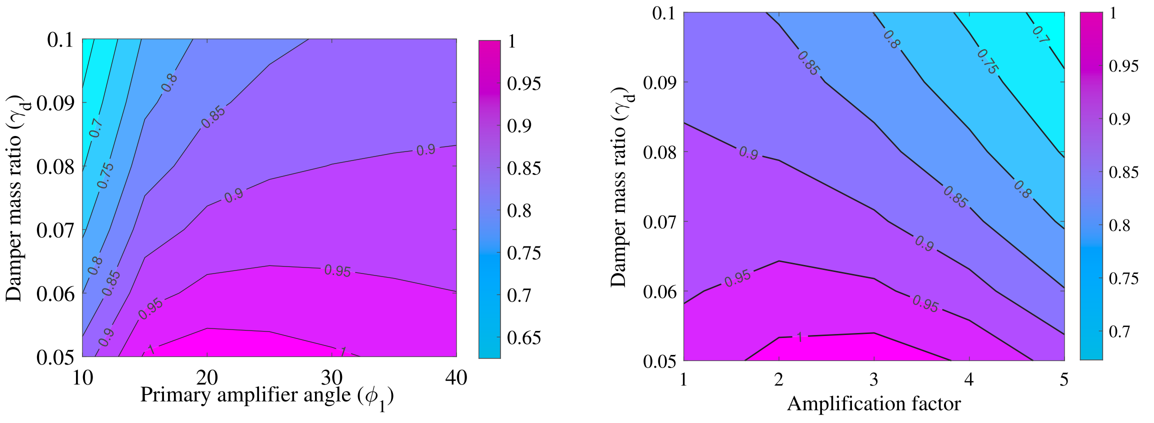

(c) NNSIATMFD: $\phi_2 = 45°, \phi_3 = 45°$ (d) NLSIATMFD

Fig. 2. Contours of the optimal frequency ratio of (a) NSIATMFD, (b) NCSIATMFD, (c) NNSIATMFD, and (d) NLSIATMFD. Eq. (16) has been applied to these graphs. The values of other system parameters are considered: $\gamma_k = 0.1$ and $\gamma_a = 0.01$.

of the main structure has been modified as

$$X_s = \frac{V_s}{V_g} = \frac{\begin{matrix} -2\mu^2 q\xi_d\gamma_d\gamma_m^2\omega_d - \kappa\mu\gamma_d\gamma_k\gamma_m\omega_d^2 - 4\mu q\xi_d\gamma_d\gamma_m\omega_d - \kappa\gamma_d\gamma_k\omega_d^2 \\ -2\mu q\xi_d\gamma_m\omega_d - \mu\gamma_d\gamma_m\omega_d^2 - \kappa\gamma_k\omega_d^2 - \mu q^2\gamma_m - 2\gamma_d\xi_d\omega_d q \\ -2\xi_d\omega_d q - \gamma_d\omega_d^2 - q^2 - \omega_d^2 \end{matrix}}{\Delta_e}. \tag{10}$$

The denominator of Eq. (10) has been derived as

$$\Delta_e = \begin{matrix} \left(\mu\gamma_m + 1\right) q^4 \\ + \left(2\mu^2\xi_d\gamma_d\gamma_m^2\omega_d + 4\mu\xi_d\gamma_d\gamma_m\omega_d + 2\mu\xi_d\gamma_m\omega_d + 2\xi_d\gamma_d\omega_d + 2\xi_d\omega_d \right) q^3 \\ + \left(\begin{matrix} \kappa\mu\gamma_d\gamma_k\gamma_m\omega_d^2 + \kappa\gamma_d\gamma_k\omega_d^2 + \mu\gamma_d\gamma_m\omega_d^2 + \kappa\gamma_k\omega_d^2 + \mu\gamma_m\omega_s^2 + \gamma_d\omega_d^2 \\ +\omega_d^2 + \omega_s^2 \end{matrix} \right) q^2 \\ + \left(2\mu\xi_d\gamma_m\omega_d\omega_s^2 + 2\xi_d\omega_d\omega_s^2\right) q + \kappa\gamma_k\omega_d^2\omega_s^2 + \omega_d^2\omega_s^2 \end{matrix}. \tag{11}$$

Therefore, utilising the above expressions, the standard deviation of the dynamic response of the main structure has been derived as

$$\sigma_{X_s}^2 = \frac{S_0\pi \left(\begin{matrix} \left(1 + \left(\mu\gamma_m + 1\right)\gamma_d\right)^4 \left(\kappa\gamma_k + 1\right)^2 \omega_d^4 \\ +4 \left(\begin{matrix} \left(\mu\gamma_m + 1\right)\left(\mu\,\xi_d^2\gamma_m + \frac{1}{4}\kappa\gamma_k + \xi_d^2 + \frac{1}{4}\right)\gamma_d \\ +\mu\,\xi_d^2\gamma_m - \frac{\kappa\gamma_k}{2} + \xi_d^2 - \frac{1}{2} \end{matrix} \right) \\ \omega_s^2 \left(\mu\gamma_m + 1\right)\left(1 + \left(\mu\gamma_m + 1\right)\gamma_d\right)^2 \omega_d^2 \\ +\omega_s^4 \left(\mu\gamma_m + 1\right)^2 \end{matrix} \right)}{2\omega_d\xi_d\left(\mu\gamma_m + 1\right)^3 \gamma_d\omega_s^6}. \tag{12}$$

Eq. (12) has been differentiated with respect to the damping ratio and natural frequency of the dampers and the mathematical expressions are derived as

$$\frac{\partial\sigma_{X_s}^2}{\partial\xi_d} = 0 \quad \text{and} \quad \frac{\partial\sigma_{X_s}^2}{\partial\omega_d} = 0. \tag{13}$$

Eq. (12) has been substituted in the first expression of Eq. (13). The exact closed-form expression for the damping ratio of the damper has been derived as

$$\xi_d = \sqrt{\frac{\begin{matrix} \left(1 + \left(\mu\gamma_m + 1\right)\gamma_d\right)^4 \left(\kappa\gamma_k + 1\right)^2 \omega_d^4 \\ + \left(-2 + \left(\mu\gamma_m + 1\right)\gamma_d\right)\left(\mu\gamma_m + 1\right)\left(1 + \left(\mu\gamma_m + 1\right)\gamma_d\right)^2 \omega_s^2 \left(\kappa\gamma_k + 1\right)\omega_d^2 \\ +\omega_s^4\left(\mu\gamma_m + 1\right)^2 \end{matrix}}{4\omega_s^2\omega_d^2\left(\mu\gamma_m + 1\right)^2\left(\mu\gamma_d\gamma_m + \gamma_d + 1\right)^3}}. \tag{14}$$

Eq. (14) represents the closed-form expression of the damping ratio of the novel dampers and this expression has been substituted in Eq. (12). Accordingly, the modified standard deviation of the dynamic response of the main structure has been derived as

$$\sigma_{X_s}^2 = \frac{2S_0\pi \left(\begin{matrix} \left(1 + \left(\mu\gamma_m + 1\right)\gamma_d\right)^4 \left(\kappa\gamma_k + 1\right)^2 \omega_d^4 \\ + \left(-2 + \left(\mu\gamma_m + 1\right)\gamma_d\right)\left(\mu\gamma_m + 1\right) \\ \left(1 + \left(\mu\gamma_m + 1\right)\gamma_d\right)^2 \omega_s^2 \left(\kappa\gamma_k + 1\right)\omega_d^2 \\ +\omega_s^4\left(\mu\gamma_m + 1\right)^2 \end{matrix} \right)}{\omega_d\left(\mu\gamma_m + 1\right)^3\gamma_d\omega_s^6 \sqrt{\frac{\begin{matrix} \left(1 + \left(\mu\gamma_m + 1\right)\gamma_d\right)^4 \left(\kappa\gamma_k + 1\right)^2 \omega_d^4 \\ + \left(-2 + \left(\mu\gamma_m + 1\right)\gamma_d\right)\left(\mu\gamma_m + 1\right) \\ \left(1 + \left(\mu\gamma_m + 1\right)\gamma_d\right)^2 \omega_s^2 \left(\kappa\gamma_k + 1\right)\omega_d^2 \\ +\omega_s^4\left(\mu\gamma_m + 1\right)^2 \end{matrix}}{\omega_s^2\omega_d^2(\mu\gamma_m+1)^2(\mu\gamma_d\gamma_m+\gamma_d+1)^3}}}. \tag{15}$$

Eq. (15) has been substituted in the second expression of the Eq. (13). Accordingly, the optimal natural frequency of the damper has been derived and expressed as

$$\left(\omega_d\right)_{\text{opt}} = \frac{\sqrt{2\left(\kappa\gamma_k + 1\right)\left(2 - \mu^2\gamma_d\gamma_m^2 - 2\mu\gamma_d\gamma_m + 2\mu\gamma_m - \gamma_d\right)}\,\omega_s}{2\left(\kappa\gamma_k + 1\right)\left(\mu\gamma_d\gamma_m + \gamma_d + 1\right)}. \tag{16}$$

Eq. (16) has been substituted in Eq. (14) to derive the exact closed-form expression for the optimal damping ratio of the damper and expressed as

$$\left(\xi_d\right)_{\text{opt}} = \frac{\sqrt{2}\sqrt{\frac{(\kappa\gamma_k+1)(\mu\gamma_d\gamma_m+\gamma_d-4)\gamma_d}{(\mu\gamma_d\gamma_m+\gamma_d-2)(\mu\gamma_d\gamma_m+\gamma_d+1)}}}{4}. \tag{17}$$

Further, Eq. (8), with $\xi_s = 0$ and Eq. (11) are utilised to derive the standard deviation of the velocity response of novel dampers and expressed as

$$\sigma_{\dot{v}_d}^2 = \frac{\left(\mu\gamma_m\gamma_d + \gamma_d + 1\right)S_0\pi}{2\left(\mu\gamma_m + 1\right)\xi_d\gamma_d\omega_d}. \tag{18}$$

Eq. (16) is utilised to conduct a parametric study for the tuning ratio of each novel damper. The contour plots in Fig. 2 illustrate the optimal frequency ratio for various designs of inertial amplifier friction tuned mass dampers under different configurations. In Fig. 2(a) and Fig. 2(b), the NSIATMFD and NCSIATMFD reveal that increasing the amplifier angle leads to higher optimal frequency ratios, indicating better performance. Fig. 2(c), which represents the NNSIATMFD, shows that the angle of the primary amplifier and the angle of the secondary influence significantly the optimal frequency ratio. Fig. 2(d) highlights the NLSIATMFD, where the amplification factor has a dominant influence on frequency ratio, exhibiting an increasing trend as the factor grows. Across all configurations, the damper mass ratio consistently impacts the optimal frequency ratio, with higher mass ratios generally enhancing damping performance. These results underscore the importance of tuning the design parameters to achieve optimal vibration mitigation, with each type of damper exhibiting unique sensitivities to the amplifier and system parameters. The inertial amplification factor for NCSIATMFD is derived as

$$\Gamma_c = \frac{m_e}{m_d} = 1 + \frac{\gamma_m}{8}\left(\cot^2\phi\left(1 + \tan^2\theta\right)\right). \tag{19}$$

The inertial amplification factor for conventional amplifier [22] is derived as

$$\Gamma_d = \frac{m_e}{m_d} = 1 + \frac{\gamma_m}{2}\left(1 + \cot^2\phi\right). \tag{20}$$

Eq. (20) and Eq. (19) have been compared. The condition for the NCSIATMFD to surpass the conventional amplifier can be expressed as $\Gamma_c > \Gamma_d$. Substituting the respective expressions, this condition becomes:

$$\frac{\left(\cot^2\phi\left(1 + \tan^2\theta\right)\right)}{8} > \frac{\left(1 + \cot^2\phi\right)}{2}. \tag{21}$$

From Eq. (21), the necessary condition for the secondary amplifier angle of NCSIATMFD θ has been derived as:

$$\tan^2\theta > \left(3 + 4\tan^2\phi\right). \tag{22}$$

This condition is in addition to $\phi < 45°$, which is required for inertial amplification in the conventional amplifier, as the primary amplifier angle is typically chosen to be small, $\tan^2\phi \rightsquigarrow 0$. Hence, the base value of θ required for the NCSIATMFD to exceed the performance of the conventional amplifier is:

$$\tan\theta > \sqrt{3} \quad \text{or} \quad \theta > 60°. \tag{23}$$

In Fig. 3, the inertial amplification factor of the compound amplifier is analysed for various parameter values, focusing on the effect of the secondary amplifier angle, θ. The results indicate that when $\theta > 60°$, the compound amplifier outperforms the conventional design in terms of amplification. Additionally, the figure reveals a unique design advantage: for a specific target inertial amplification, such as 30, there exists a range of ϕ and θ combinations capable of achieving the desired

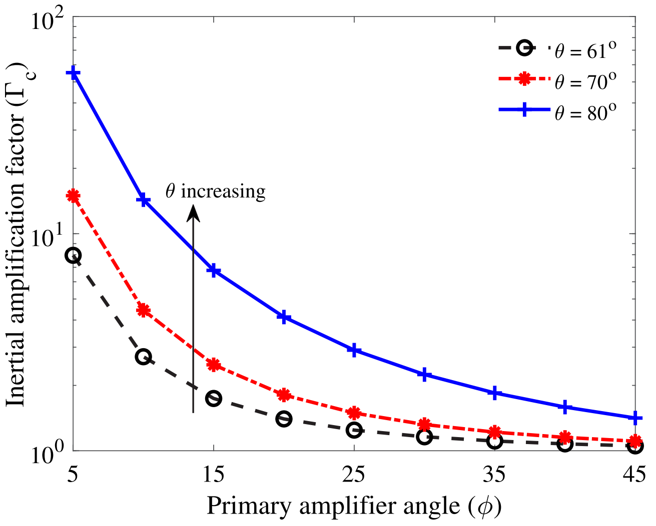

Fig. 3. Inertial amplification as a function of primary amplifier angle ϕ for the NCSIATMFD across different combinations of θ. The mass factor γ_m is valued at 0.1. Eq. (19) is employed to achieve this graph.

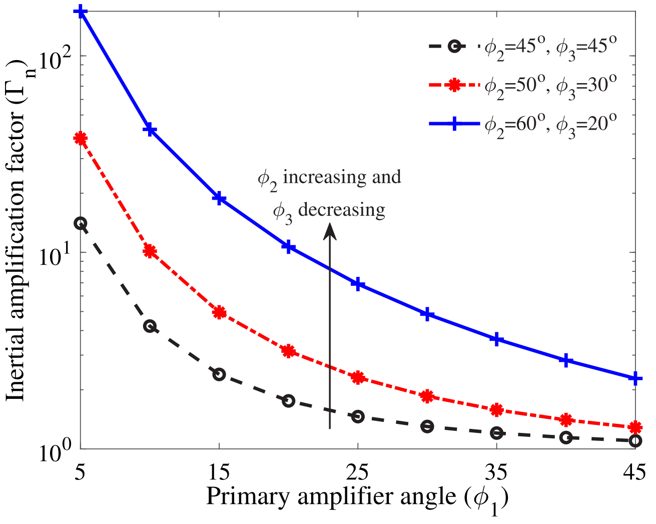

Fig. 4. Inertial amplification as a function of primary amplifier angle ϕ_1 for the NNSIATMFD across different combinations of ϕ_2 and ϕ_3. The mass factor γ_m is valued at 0.1. Eq. (25) is employed to achieve this graph.

outcome. This design flexibility provides greater freedom in addressing practical limitations while maintaining optimal performance.

The primary amplifier angle is often selected to be minimal, resulting in $\tan^2\phi_1 \rightsquigarrow 0$ to achieve significant amplification from the NNSIATMFD. Consequently, the values of ϕ_2 and ϕ_3, necessary for the nested amplifier to surpass the conventional amplifier, are

$$\tan\phi_2 \geq 1 \quad \text{or} \quad \phi_2 \geq 45^\circ \quad \text{and} \quad \cot\phi_3 \geq 1 \quad \text{or} \quad \phi_3 \leq 45^\circ. \tag{24}$$

In addition to the requirement $\phi_1 < 45^\circ$ for inertial amplification in a conventional amplifier [22], these conditions must also be satisfied. The inertial amplification factor of the NNSIATMFD has been derived as

$$\Gamma_n = \frac{m_e}{m_d} = 1 + \frac{\gamma_m}{2}\left(1 + \cot^2\phi_3\right)\cot^2\phi_1\tan^2\phi_2. \tag{25}$$

The inertial amplification factor of the NNSIATMFD is compared for various parameter values in Fig. 4. Amplifications for three distinct combinations of the angles ϕ_2 and ϕ_3 are shown. The findings unequivocally demonstrate that when $\phi_2 \geq 45^\circ$ and $\phi_3 \leq 45^\circ$, the amplification of the nested amplifier significantly exceeds that of its traditional equivalent. The findings in Fig. 4 provide an intriguing alternative that is unattainable with the standard amplifier. For a specified goal inertial amplification of 30, many combinations of ϕ_1, ϕ_2, and ϕ_3 may be chosen. This provides more potential for the design to meet any practical limitations.

The contour plots in Fig. 5 illustrate the optimal damping ratio for different types of inertial amplifier friction tuned mass dampers, demonstrating the influence of design parameters on damping efficiency. In Fig. 5(a), the NSIATMFD shows a significant increase in the optimal damping ratio with larger amplifier angles and higher damper mass ratios. Similarly, in Fig. 5(b), the NCSIATMFD reveals a similar trend, with larger amplifier angles leading to higher damping ratios, particularly for higher damper mass ratios. Fig. 5(c) highlights the NNSIATMFD, where the primary amplifier angle is a critical parameter, with the contours showing a steep gradient in optimal damping as it increases. Lastly, in Fig. 5(d), the NLSIATMFD demonstrates that increasing the amplification factor positively influences the damping ratio, particularly at lower damper mass ratios. Overall, these results emphasise the necessity of fine-tuning amplifier angles, mass ratios, and amplification factors to achieve the desired damping performance across various damper configurations. Each design presents unique sensitivities, offering flexible options for vibration control.

2.2. H_∞ optimisation

Further, the exact closed-form expressions for the optimal design parameters of the damper are derived using the H_∞ optimisation method. It is considered that the controlled structure is subjected to harmonic excitation. To perform that the transfer function in Eq. (6) has been non-dimensionalised by dividing it by ω_s^2 and expressed as

$$\begin{gathered}\begin{bmatrix} -\eta^2+1 & A_{12} \\ -\gamma_d\left(\gamma_m\mu+1\right)\eta^2 & A_{22}\end{bmatrix}\begin{Bmatrix} V_s \\ V_d\end{Bmatrix} = -\begin{bmatrix} 1 \\ \gamma_d\left(\mu\gamma_m+1\right)\end{bmatrix}\frac{V_g}{\omega_s^2},\\ A_{12} = -2\,\mathrm{i}\gamma_d\left(\gamma_m\mu+1\right)\xi_d\eta_d\eta - \gamma_d\eta_d^2\left(\gamma_k\kappa+1\right),\\ A_{22} = -\gamma_d\left(\gamma_m\mu+1\right)\eta^2 + 2\,\mathrm{i}\gamma_d\left(\gamma_m\mu+1\right)\xi_d\eta_d\eta + \gamma_d\eta_d^2\left(\gamma_k\kappa+1\right).\end{gathered} \tag{26}$$

where $\eta = \omega/\omega_s$ defines the frequency ratio. The dynamic response of the main structure has been derived as

$$\begin{aligned} X_s &= \left(\frac{V_s}{V_g}\right)\omega_s^2 \\ &= \frac{\begin{gathered}\eta_d^2\kappa\mu\gamma_d\gamma_k\gamma_m + \eta_d^2\kappa\gamma_d\gamma_k + \eta_d^2\mu\gamma_d\gamma_m - \eta^2\mu\gamma_m + \eta_d^2\kappa\gamma_k \\ +\eta_d^2\gamma_d - \eta^2 + \eta_d^2 \\ +\mathrm{i}\xi_d\left(2\eta\eta_d\mu^2\gamma_d\gamma_m^2 + 4\eta\eta_d\mu\gamma_d\gamma_m + 2\eta\eta_d\mu\gamma_m + 2\eta\eta_d\gamma_d + 2\eta_d\eta\right)\end{gathered}}{\Delta_e}.\end{aligned} \tag{27}$$

The dynamic response of the damper has been derived as

$$X_d = \left(\frac{V_d}{V_g}\right)\omega_s^2 = \frac{\gamma_m\mu+1}{\Delta_e}. \tag{28}$$

The denominator of Eq. (27) and Eq. (28) has been derived as

$$\Delta_e = \begin{gathered}\eta^2\eta_d^2\kappa\mu\gamma_d\gamma_k\gamma_m + \eta^2\eta_d^2\kappa\gamma_d\gamma_k + \eta^2\eta_d^2\mu\gamma_d\gamma_m - \eta^4\mu\gamma_m + \eta^2\eta_d^2\kappa\gamma_k \\ +\eta^2\eta_d^2\gamma_d - \eta^4 + \eta^2\eta_d^2 + \eta^2\mu\gamma_m - \eta_d^2\kappa\gamma_k + \eta^2 - \eta_d^2 \\ +\mathrm{i}\xi_d\begin{pmatrix} 2\eta^3\eta_d\mu^2\gamma_d\gamma_m^2 + 4\eta^3\eta_d\mu\gamma_d\gamma_m + 2\eta^3\eta_d\mu\gamma_m \\ +2\eta^3\eta_d\gamma_d + 2\eta^3\eta_d - 2\eta\eta_d\mu\gamma_m - 2\eta_d\eta\end{pmatrix}\end{gathered}. \tag{29}$$

The resultant of Eq. (27) has been applied to derive constraints and expressed as

$$|X_s| = \sqrt{\frac{R_1^2 + \xi_d^2 R_2^2}{R_3^2 + \xi_d^2 R_4^2}}. \tag{30}$$

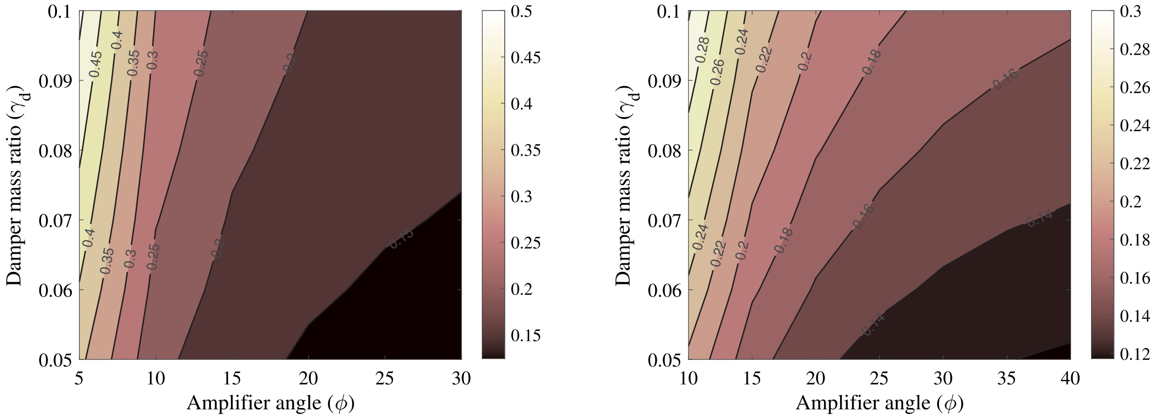

(a) NSIATMFD

(b) NCSIATMFD: $\theta = 64°$

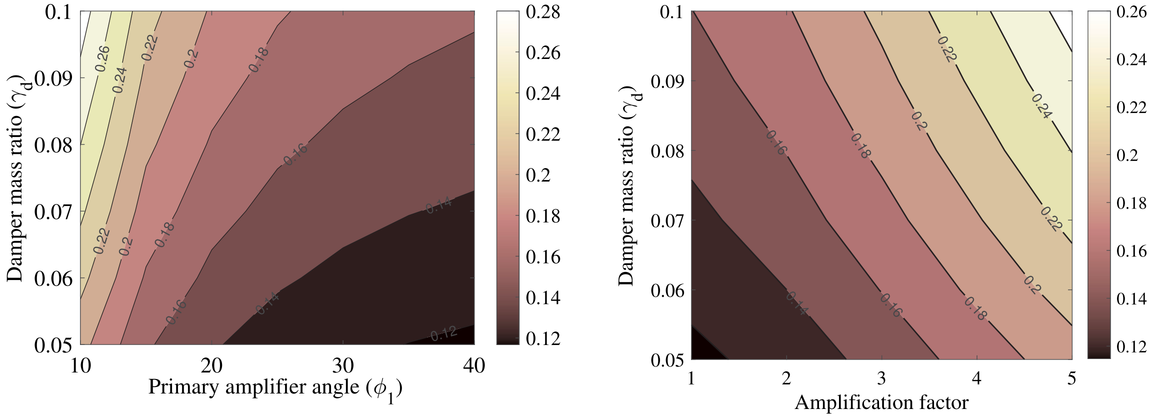

(c) NNSIATMFD: $\phi_2 = 45°, \phi_3 = 45°$

(d) NLSIATMFD

Fig. 5. Contours of the optimal damping ratio of (a) NSIATMFD, (b) NCSIATMFD, (c) NNSIATMFD, and (d) NLSIATMFD. Eq. (17) has been applied for these graphs. The values of other system parameters are considered: $\gamma_k = 0.1$ and $\gamma_a = 0.01$.

The closed-form expressions for R_1 to R_4 have been derived as

$$\begin{aligned}
R_1 &= \eta_d^2\kappa\mu\gamma_d\gamma_k\gamma_m + \eta_d^2\kappa\gamma_d\gamma_k + \eta_d^2\mu\gamma_d\gamma_m - \eta^2\mu\gamma_m + \eta_d^2\kappa\gamma_k + \eta_d^2\gamma_d - \eta^2 + \eta_d^2,\\
R_2 &= 2\eta\eta_d\mu^2\gamma_d\gamma_m^2 + 4\eta\eta_d\mu\gamma_d\gamma_m + 2\eta\eta_d\mu\gamma_m + 2\eta\eta_d\gamma_d + 2\eta\eta_d,\\
R_3 &= \begin{array}{c} \eta^2\eta_d^2\kappa\mu\gamma_d\gamma_k\gamma_m + \eta^2\eta_d^2\kappa\gamma_d\gamma_k + \eta^2\eta_d^2\mu\gamma_d\gamma_m - \eta^4\mu\gamma_m + \eta^2\eta_d^2\kappa\gamma_k \\ +\eta^2\eta_d^2\gamma_d - \eta^4 + \eta^2\eta_d^2 + \eta^2\mu\gamma_m - \eta_d^2\kappa\gamma_k + \eta^2 - \eta_d^2 \end{array},\\
R_4 &= \begin{array}{c} 2\eta^3\eta_d\mu^2\gamma_d\gamma_m^2 + 4\eta^3\eta_d\mu\gamma_d\gamma_m + 2\eta^3\eta_d\mu\gamma_m \\ +2\eta^3\eta_d\gamma_d + 2\eta^3\eta_d - 2\eta\eta_d\mu\gamma_m - 2\eta\eta_d \end{array}.
\end{aligned} \tag{31}$$

Two constraints are derived as follows.

$$\left.\frac{R_1}{R_2}\right|_{\eta_j} = \left.\frac{R_3}{R_4}\right|_{\eta_j} \quad \text{and} \quad \left.\frac{R_3}{R_4}\right|_{\eta_1} = \left.\frac{R_3}{R_4}\right|_{\eta_2}. \tag{32}$$

Eq. (31) has been substituted in the first constraint of Eq. (32). As a result, an equation has been derived which contains the optimal natural frequency of the dampers and expressed as

$$\begin{array}{c}
\left(2\mu^2\gamma_d\gamma_m^2 + 4\mu\gamma_d\gamma_m + 2\mu\gamma_m + 2\gamma_d + 2\right)\eta^4 + \\
\left(\begin{array}{c} -2\eta_d^2\kappa\mu^2\gamma_d^2\gamma_k\gamma_m^2 - 4\eta_d^2\kappa\mu\gamma_d^2\gamma_k\gamma_m - 2\eta_d^2\mu^2\gamma_d^2\gamma_m^2 - 4\eta_d^2\kappa\mu\gamma_d\gamma_k\gamma_m \\ -2\eta_d^2\kappa\gamma_d^2\gamma_k - 4\eta_d^2\mu\gamma_d^2\gamma_m - 4\eta_d^2\kappa\gamma_d\gamma_k - 4\eta_d^2\mu\gamma_d\gamma_m - \mu^2\gamma_d\gamma_m^2 \\ -2\eta_d^2\kappa\gamma_k - 2\eta_d^2\gamma_d^2 - 4\eta_d^2\gamma_d - 2\mu\gamma_d\gamma_m - 2\eta_d^2 - 2\mu\gamma_m - \gamma_d - 2 \end{array}\right)\eta^2 + \quad = 0. \\
2\eta_d^2\kappa\mu\gamma_d\gamma_k\gamma_m + 2\eta_d^2\kappa\gamma_d\gamma_k + 2\eta_d^2\mu\gamma_d\gamma_m + 2\eta_d^2\kappa\gamma_k + 2\eta_d^2\gamma_d + 2\eta_d^2
\end{array} \tag{33}$$

The summation of two roots from the Eq. (33) has been derived as

$$\eta_1^2 + \eta_2^2 = \frac{\left(\begin{array}{c} 2\eta_d^2\left(\mu\gamma_m + 1\right)^2\left(\kappa\gamma_k + 1\right)\gamma_d^2 \\ +\left(\mu\gamma_m + 1\right)\left(\mu\gamma_m + 1 + \left(4\kappa\gamma_k + 4\right)\eta_d^2\right)\gamma_d \\ +2\mu\gamma_m + 2 + \left(2\kappa\gamma_k + 2\right)\eta_d^2 \end{array}\right)}{2\left(1 + \left(\mu\gamma_m + 1\right)\gamma_d\right)\left(\mu\gamma_m + 1\right)}. \tag{34}$$

Eq. (31) has been substituted in the second constraint of Eq. (32) and as a result, the summation of two roots is derived as

$$\eta_1^2 + \eta_2^2 = \frac{2}{\mu\gamma_d\gamma_m + \gamma_d + 1}. \tag{35}$$

Eq. (34) and Eq. (35) are equated and the exact closed-form expression for the optimal natural frequency of the damper has been derived as

$$\begin{aligned}
&\left(\begin{array}{c} 2\kappa\mu^2\gamma_d^2\gamma_k\gamma_m^2 + 4\kappa\mu\gamma_d^2\gamma_k\gamma_m + 2\mu^2\gamma_d^2\gamma_m^2 + 4\kappa\mu\gamma_d\gamma_k\gamma_m + 2\kappa\gamma_d^2\gamma_k \\ +4\mu\gamma_d^2\gamma_m + 4\kappa\gamma_d\gamma_k + 4\mu\gamma_d\gamma_m + 2\kappa\gamma_k + 2\gamma_d^2 + 4\gamma_d + 2 \end{array}\right)\eta_d^2 \\
&+ \mu^2\gamma_d\gamma_m^2 + 2\mu\gamma_d\gamma_m - 2\mu\gamma_m + \gamma_d - 2 = 0, \\
&\left(\eta_d\right)_{\text{opt}} = \frac{\sqrt{\begin{array}{c} 4 - 2\kappa\mu^2\gamma_d\gamma_k\gamma_m^2 - 4\kappa\mu\gamma_d\gamma_k\gamma_m - 2\mu^2\gamma_d\gamma_m^2 + 4\kappa\mu\gamma_k\gamma_m \\ -2\kappa\gamma_d\gamma_k - 4\mu\gamma_d\gamma_m + 4\kappa\gamma_k + 4\mu\gamma_m - 2\gamma_d \end{array}}}{2\left(\kappa\gamma_k + 1\right)\left(\mu\gamma_d\gamma_m + \gamma_d + 1\right)}.
\end{aligned} \tag{36}$$

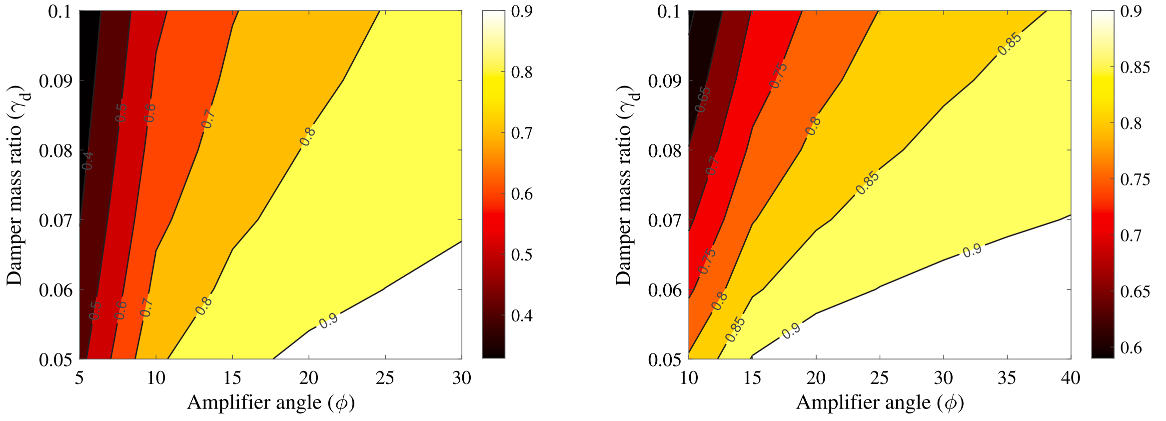

(a) NSIATMFD

(b) NCSIATMFD: $\theta = 64°$

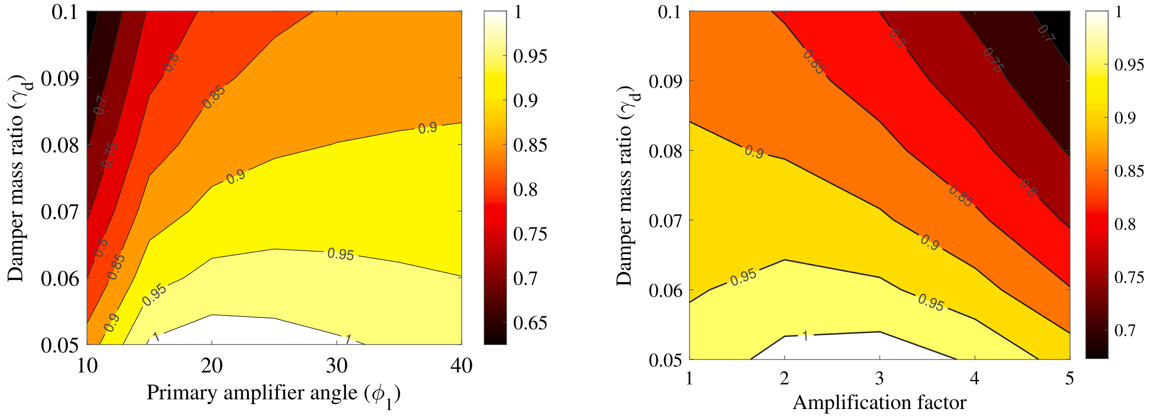

(c) NNSIATMFD: $\phi_2 = 45°, \phi_3 = 45°$

(d) NLSIATMFD

Fig. 6. Contours of the optimal frequency ratio of (a) NSIATMFD, (b) NCSIATMFD, (c) NNSIATMFD, and (d) NLSIATMFD. Eq. (36) has been applied for these graphs. The values of other system parameters are considered: $\gamma_k = 0.1$ and $\gamma_a = 0.01$.

The individual expression for each root, i.e. η_1^2 and η_2^2, has been derived as

$$\eta_{1,2}^2 = \frac{1 + \mu\gamma_m \pm \sqrt{\begin{array}{c} -\eta_d^2\kappa\mu^3\gamma_d^2\gamma_k\gamma_m^3 - 3\eta_d^2\kappa\mu^2\gamma_d^2\gamma_k\gamma_m^2 - \eta_d^2\mu^3\gamma_d^2\gamma_m^3 \\ -2\eta_d^2\kappa\mu^2\gamma_d\gamma_k\gamma_m^2 - 3\eta_d^2\kappa\mu\gamma_d^2\gamma_k\gamma_m - 3\eta_d^2\mu^2\gamma_d^2\gamma_m^2 \\ -4\eta_d^2\kappa\mu\gamma_d\gamma_k\gamma_m - 2\eta_d^2\mu^2\gamma_d\gamma_m^2 - \eta_d^2\kappa\mu\gamma_k\gamma_m \\ -\eta_d^2\kappa\gamma_d^2\gamma_k - 3\eta_d^2\mu\gamma_d^2\gamma_m - 2\eta_d^2\kappa\gamma_d\gamma_k - 2\eta_d^2\gamma_d \\ -4\eta_d^2\mu\gamma_d\gamma_m - \eta_d^2\kappa\gamma_k - \eta_d^2\mu\gamma_m - \eta_d^2\gamma_d^2 + \mu^2\gamma_m^2 \\ -\eta_d^2 + 2\mu\gamma_m + 1 \end{array}}}{\mu^2\gamma_d\gamma_m^2 + 2\mu\gamma_d\gamma_m + \mu\gamma_m + \gamma_d + 1}. \tag{37}$$

The closed-form expression for the optimal damping ratio of the damper has been derived by formulating a mathematical expression and expressed as

$$\left.\frac{\partial |X_s|^2}{\partial \eta^2}\right|_{\eta_{1,2}^2} = 0 \quad \text{and} \quad (\xi_d)_{\text{opt}} = \sqrt{\frac{\xi_{d1}^2 + \xi_{d2}^2}{2}}. \tag{38}$$

Eq. (30) has been substituted in the first expression of Eq. (38) and the closed-form expression for optimal damping ratio of the damper has been derived as

$$Z_1\xi_d^4 + Z_2\xi_d^2 + Z_3 = 0,$$
$$\left(\xi_{d1,d2}\right)_{\eta_{1,2}^2}^2 = \frac{-Z_2 \pm \sqrt{Z_2^2 - 4Z_1Z_3}}{2Z_1}. \tag{39}$$

The closed-form expressions for Z_1, Z_2, and Z_3 have been derived and listed in Appendix. Fig. 6 illustrates the contours of the optimal frequency ratio across four configurations of novel dampers: Fig. 6(a) NSIATMFD, Fig. 6(b) NCSIATMFD, Fig. 6(c) NNSIATMFD, and Fig. 6(d) NLSIATMFD. Each plot evaluates the interplay between the damper mass ratio and design parameters such as the amplifier angle or amplification factor. The results reveal that higher damper mass ratios generally lead to an increased optimal frequency ratio, improving the system's vibration mitigation capabilities. Specifically, the NSIATMFD and NCSIATMFD configurations show smoother transitions in frequency ratio contours, indicating a more robust performance over a range of amplification parameters. In contrast, the NNSIATMFD configuration demonstrates sharp gradients, suggesting greater sensitivity to variations in the primary amplifier angle, especially when $\phi_2 = 70°$ and $\phi_3 = 15°$. The NLSIATMFD achieves the highest optimal frequency ratio (~ 1) at high amplification factors, highlighting its superior tuning capability for larger vibration amplitudes. Overall, these findings emphasise the critical role of system design parameters in optimising the performance of novel dampers, providing a valuable guide for tailored vibration control applications.

The contours in Fig. 7 present the optimal damping ratio for different configurations of novel dampers: Fig. 7(a) NSIATMFD, Fig. 7(b) NCSIATMFD, Fig. 7(c) NNSIATMFD, and Fig. 7(d) NLSIATMFD. The damping ratio contours are mapped as a function of the damper mass ratio and system-specific parameters such as amplifier angle or amplification factor. Across all configurations, the damping ratio improves with higher values of the damper mass ratio, confirming its crucial

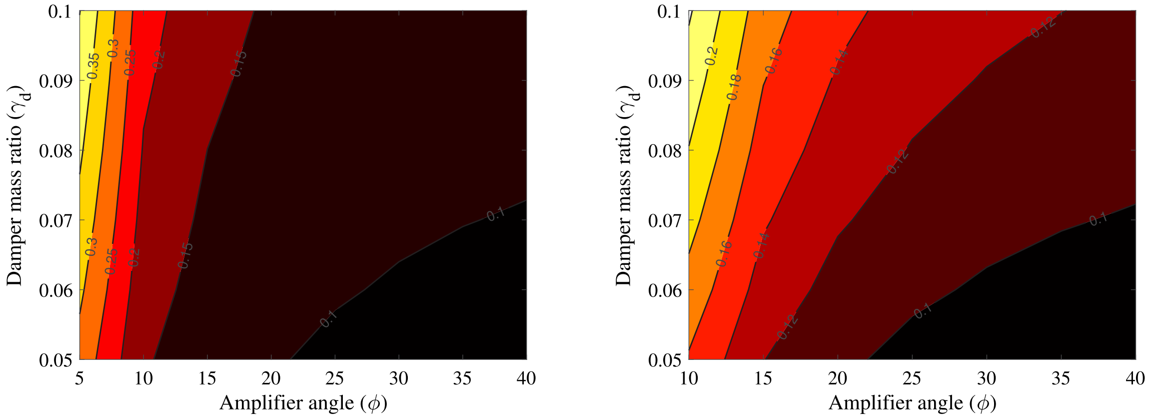

(a) NSIATMFD (b) NCSIATMFD: $\theta = 64°$

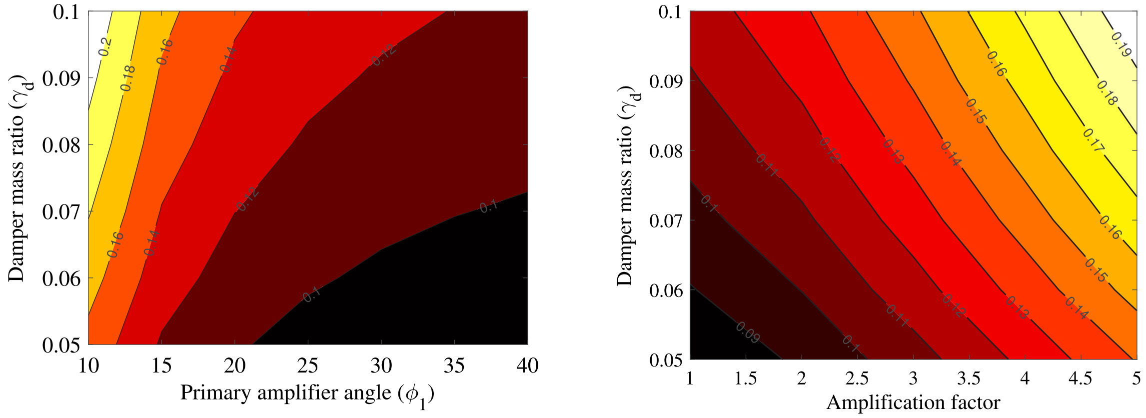

(c) NNSIATMFD: $\phi_2 = 45°, \phi_3 = 45°$ (d) NLSIATMFD

Fig. 7. Contours of the optimal damping ratio of (a) NSIATMFD, (b) NCSIATMFD, (c) NNSIATMFD, and (d) NLSIATMFD. Eq. (38) has been applied for these graphs. The values of other system parameters are considered: $\gamma_k = 0.1$ and $\gamma_a = 0.01$.

role in energy dissipation. The NSIATMFD and NCSIATMFD show smoother contour transitions, demonstrating consistent damping behaviour over wider ranges of amplifier angles, with the NCSIATMFD achieving slightly better damping efficiency at specific amplifier angles ($\theta = 64°$). The NNSIATMFD configuration exhibits a sharp reduction in damping efficiency outside certain critical primary amplifier angles, making its performance highly sensitive to design variations. The NLSIATMFD configuration highlights a nearly uniform improvement in the damping ratio with increasing amplification factor, achieving a maximum damping ratio of $\sim$ 0.2 for high amplification factors. These observations emphasise the design flexibility of NLSIATMFD for effective damping in diverse structural applications.

3. Dynamic response evaluation

The efficiency of the optimal design parameters is investigated by obtaining dynamic responses of the controlled structures where the optimal tuning and damping ratios are applied inside the governing equations of motion. In addition, the damping ratio of the main structure is considered as 0.01, i.e., $\xi_s = 0.01$ (see Table 3).

Table 3
The structural parameter of the main structure.

Main structure	Governing system parameter	Value
		ξ_s
SDOF system	Damping ratio	0.01

3.1. Frequency domain responses

First, harmonic excitation is applied at the base. The H_2 and H_∞ optimised conventional tuned mass dampers are considered in this study to conduct a comparative study between the novel and conventional dampers in terms of vibration reduction. The total static mass of all dampers is maintained the same to make a fair comparison, i.e., Conventional tuned mass damper one (TMD1): damper mass ratio ($\tilde{\gamma}_d$) = 0.09, Conventional tuned mass damper two (TMD2): damper mass ratio ($\tilde{\gamma}_d$) = 0.09, NSIATMFD: damper mass ratio (γ_d) = 0.07, (γ_a) = 0.01 $\phi = 40^o$; NCSIATMFD: γ_d = 0.07, (γ_a) = 0.01, $\phi = 40^o$, $\theta = 64^o$; NNSIATMFD: γ_d = 0.07, (γ_a) = 0.01, $\phi_1 = 40^o$, $\phi_2 = 45^o$, $\phi_3 = 45^o$, and NLSIATMFD: γ_d = 0.08, (γ_a) = 0.01, $b_1/a_1 = 1$, $b_2/a_2 = 1$. These values are substituted in Eq. (16) and Eq. (17) to obtain the optimal frequency and damping ratios of the H_2 optimised novel dampers. To obtain optimal design parameters for the conventional dampers, the value of $\tilde{\gamma}_d$ is substituted into the well-established closed-form expressions derived by Warburton et al. [23], Zilletti [24], Iwata [25], and Warburton et al. [23]. Accordingly, The governing system parameters of the H_2 optimised tuned mass dampers are listed in Table 4.

Further, for H_∞ optimised dampers, the total static mass of all dampers is maintained the same to make a fair comparison, i.e., Conventional tuned mass damper one (TMD1): damper mass ratio ($\tilde{\gamma}_d$) = 0.09, Conventional tuned mass damper two (TMD2): damper mass ratio ($\tilde{\gamma}_d$) = 0.09, NSIATMFD: damper mass ratio (γ_d) = 0.07, (γ_a) = 0.01

Table 4
H_2 optimised design parameters.

System	Introduced by	H_2 optimisation	
		η_d	ξ_d
NSIATMFD	Eq. (16) and Eq. (17)	0.917102	0.137348
NCSIATMFD	Eq. (16) and Eq. (17)	0.901185	0.137912
NNSIATMFD	Eq. (16) and Eq. (17)	0.926457	0.137253
NLSIATMFD	Eq. (16) and Eq. (17)	0.924723	0.13489
TMD1	Warburton et al [23],Zilletti [24]	$\frac{1}{\sqrt{1+\tilde{\gamma}_d}}$	$\frac{\sqrt{\tilde{\gamma}_d}}{2}$
TMD2	Iwata [25], Warburton et al [23]	$\frac{1}{1+\tilde{\gamma}_d}\sqrt{\frac{2+\tilde{\gamma}_d}{2}}$	$\sqrt{\frac{\tilde{\gamma}_d(4+3\tilde{\gamma}_d)}{8(1+\tilde{\gamma}_d)(2+\tilde{\gamma}_d)}}$

Conventional tuned mass damper one (TMD1): damper mass ratio ($\tilde{\gamma}_d$) = 0.09, Conventional tuned mass damper two (TMD2): damper mass ratio ($\tilde{\gamma}_d$) = 0.09, NSIATMFD: damper mass ratio (γ_d) = 0.07, (γ_a) = 0.01 $\phi = 40^o$; NCSIATMFD: γ_d = 0.07, (γ_a) = 0.01, $\phi = 40^o$, $\theta = 64^o$; NNSIATMFD: γ_d = 0.07, (γ_a) = 0.01, $\phi_1 = 40^o$, $\phi_2 = 45^o$, $\phi_3 = 45^o$, and NLSIATMFD: γ_d = 0.08, (γ_a) = 0.01, $b_1/a_1 = 1$, $b_2/a_2 = 1$.

Table 5
H_∞ optimised design parameters.

System	Introduced by	H_∞ optimisation	
		η_d	ξ_d
NSIATMFD	Eq. (36) and Eq. (38)	0.679318	0.183966
NCSIATMFD	Eq. (36) and Eq. (38)	0.691957	0.186608
NNSIATMFD	Eq. (36) and Eq. (38)	0.742293	0.181565
NLSIATMFD	Eq. (36) and Eq. (38)	0.859795	0.144566
TMD1	Ormondroyd and Den Hartog [26] Nishihara and Asami [27]	$\frac{1}{1+\tilde{\gamma}_d}$	$\sqrt{\frac{3\tilde{\gamma}_d}{8(1+\tilde{\gamma}_d)}}$
TMD2	Krenk [28]	$\frac{1}{1+\tilde{\gamma}_d}$	$\sqrt{\frac{\tilde{\gamma}_d}{2(1+\tilde{\gamma}_d)}}$

Conventional tuned mass damper one: damper mass ratio ($\tilde{\gamma}_d$) = 0.09, Conventional tuned mass damper two: damper mass ratio ($\tilde{\gamma}_d$) = 0.09, NSIATMFD: damper mass ratio (γ_d) = 0.07, (γ_a) = 0.01 $\phi = 10^o$; NCSIATMFD: γ_d = 0.07, (γ_a) = 0.01, $\phi = 10^o$, $\theta = 64^o$; NNSIATMFD: γ_d = 0.07, (γ_a) = 0.01, $\phi_1 = 10^o$, $\phi_2 = 45^o$, $\phi_3 = 45^o$, and NLSIATMFD: γ_d = 0.08, (γ_a) = 0.01, $b_1/a_1 = 1$, $b_2/a_2 = 2$.

$\phi = 40^o$; NCSIATMFD: $\gamma_d = 0.07$, $(\gamma_a) = 0.01$, $\phi = 40^o$, $\theta = 64^o$; NNSIATMFD: $\gamma_d = 0.07$, $(\gamma_a) = 0.01$, $\phi_1 = 40^o$, $\phi_2 = 45^o$, $\phi_3 = 45^o$, and NLSIATMFD: $\gamma_d = 0.08$, $(\gamma_a) = 0.01$, $b_1/a_1 = 1$, $b_2/a_2 = 1$. These values are substituted in Eq. (36) and Eq. (38) to obtain the optimal frequency and damping ratios of the H_∞ optimised novel dampers. To obtain optimal design parameters for the conventional dampers, the value of $\tilde{\gamma}_d$ is substituted into the well-established closed-form expressions derived by Ormondroyd and Den Hartog [26], Nishihara and Asami [27], and Krenk [28]. Accordingly, the governing system parameters of H_∞ optimised novel and conventional dampers are listed in Table 5.

The frequency domain responses are obtained using the above-mentioned design parameters and forming frequency response function. Accordingly, the dynamic responses of the structures controlled by the H_2 and H_∞ optimised novel and conventional dampers are shown in Fig. 8(a) and Fig. 8(b). The maximum displacement of the uncontrolled structure has been derived as 50. In Fig. 8(a), the maximum displacements of the main structures are controlled by H_2 optimised TMD1, TMD2, NSIATMFD, NCSIATMFD, NNSIATMFD, and NLSIATMFD have been determined as 6.8995, 6.3272, 5.3477, 5.4196, 5.2974, and 5.7782. Hence, H_2 optimised NSIATMFD, NCSIATMFD, NNSIATMFD, and NLSIATMFD are significantly 22.49%, 21.45%, 23.22%, and 16.25% superior to the H_2 optimised conventional TMD. In addition, according to Fig. 8(b), the maximum displacements of the main structures are controlled by H_∞ optimised TMD1, TMD2, NSIATMFD, NCSIATMFD, NNSIATMFD, and NLSIATMFD have been determined as 5.4249, 5.3939, 4.4027, 4.2034, 3.8777, and 5.2111. Hence, H_∞ optimised NSIATMFD, NCSIATMFD, NNSIATMFD, and NLSIATMFD are significantly 18.84%, 22.52%, 28.52%, and 3.94% superior to the H_∞ optimised conventional TMD.

Now, Clough–Penzien power spectrum, which is a modified version of the popular Kanai–Tajimi spectrum, is considered for the loading function to represent the base excitation. This consideration is helping to validate the performed methodology across a broader range of seismic excitation scenarios.

$$\ddot{v}_g = S_0 \frac{\varepsilon_f^4 + 4\zeta_f^2\varepsilon_f^2\omega^2}{\left(\varepsilon_f^2 - \omega^2\right)^2 + 4\zeta_f^2\varepsilon_f^2\omega^2} \frac{\omega^4}{\left(\varepsilon_g^2 - \omega^2\right)^2 + 4\zeta_g^2\varepsilon_g^2\omega^2}$$
$$= S_0 \frac{\varepsilon_f^4 - 4\zeta_f^2\varepsilon_f^2 q^2}{\left(\varepsilon_f^2 + q^2\right)^2 - 4\zeta_f^2\varepsilon_f^2 q^2} \frac{q^4}{\left(\varepsilon_g^2 + q^2\right)^2 - 4\zeta_g^2\varepsilon_g^2 q^2} \tag{40}$$

where S_0 and $q = \mathrm{i}\omega$ define the power spectral density for random noise. ζ_f and ε_f define the damping capacity and natural frequency of the soil layer. A second filter gives a limited power output for the ground displacement by using the parameters ε_g and ζ_g. Since the second quotient $\varepsilon_g \ll \varepsilon_f$ reaches unity very soon, the second filter only affects very low-range frequencies. The filter parameter values to study locations with firm, medium, and soft soils are taken from [29]. Firm soil is considered for this study.

The dynamic responses of the structures controlled by the H_2 and H_∞ optimised novel and conventional dampers subjected to random excitation are shown in Fig. 9(a) and Fig. 9(b). In Fig. 9(a), the maximum displacements of the main structures are controlled by H_2 optimised TMD1, TMD2, NSIATMFD, NCSIATMFD, NNSIATMFD, and NLSIATMFD have been determined as 1.0690×10^7 dB/Hz, 8.3528×10^6 dB/Hz, 5.8581×10^6 dB/Hz, 6.1718×10^6 dB/Hz, 6.5892×10^6 dB/Hz, and 7.3794×10^6 dB/Hz. Hence, H_2 optimised NSIATMFD, NCSIATMFD, NNSIATMFD, and NLSIATMFD are significantly 45.20%, 42.26%, 38.36%, and 30.96% superior to the H_2 optimised conventional TMD. In addition, according to Fig. 9(b), the maximum displacements of the main structures are controlled by H_∞ optimised TMD1, TMD2, NSIATMFD, NCSIATMFD, NNSIATMFD, and NLSIATMFD have been determined as 1.6444×10^7 dB/Hz, 6.1116×10^6 dB/Hz, 6.3325×10^6 dB/Hz, 4.4208×10^6 dB/Hz, 3.9661×10^6 dB/Hz, and 3.3336×10^6 dB/Hz. Hence, H_∞ optimised NSIATMFD, NCSIATMFD, NNSIATMFD, and NLSIATMFD are significantly 27.66%, 35.10%, 45.45%, 2.86% superior to the H_∞ optimised conventional TMD.

In addition, it is observed that the controlled curves start so high with respect to the uncontrolled response in Fig. 9. The high starting point of the controlled curves in Fig. 9 compared to the uncontrolled response can be attributed to the nature of the input excitation and the immediate engagement of the dampers. Specifically, the Clough–Penzien power spectrum introduces a broad frequency range with varying amplitudes, simulating seismic excitations that activate the dampers immediately. The initial high response reflects the transient phase, during which the dampers adapt to the input energy distribution. To provide further clarity, Fig. 10 has been included. It demonstrates the dynamic responses of the uncontrolled and controlled structures with and without the influence of the Clough–Penzien power spectrum. Fig. 10(a) depicts the system's response with the Clough–Penzien power spectrum, which models realistic seismic ground motion, accounting for both soil damping and filtering effects. This power spectrum introduces a broader frequency range and amplitude variations, reflecting the complexity of actual seismic excitations. The dampers are shown to effectively suppress vibrations, with their performance influenced by the characteristics of the input excitation. In contrast, Fig. 10(b) shows that the controlled curves start with the same amplitudes with respect to the uncontrolled response. For this figure, it is considered that the controlled structures are subjected to random excitations without considering the Clough–Penzien spectrum. Here, the response lacks the specific spectral characteristics imparted by the power spectrum, offering a baseline comparison of the dampers' performance under

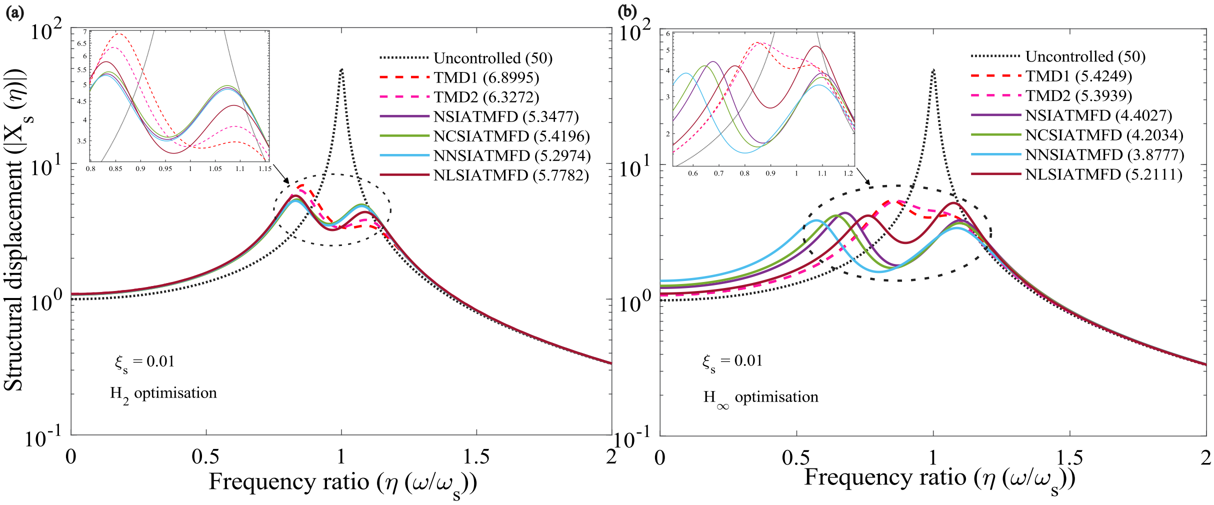

Fig. 8. The dynamic responses of the main structure are controlled by the (a) H_2 and (b) H_∞ optimised dampers subjected to harmonic excitation.

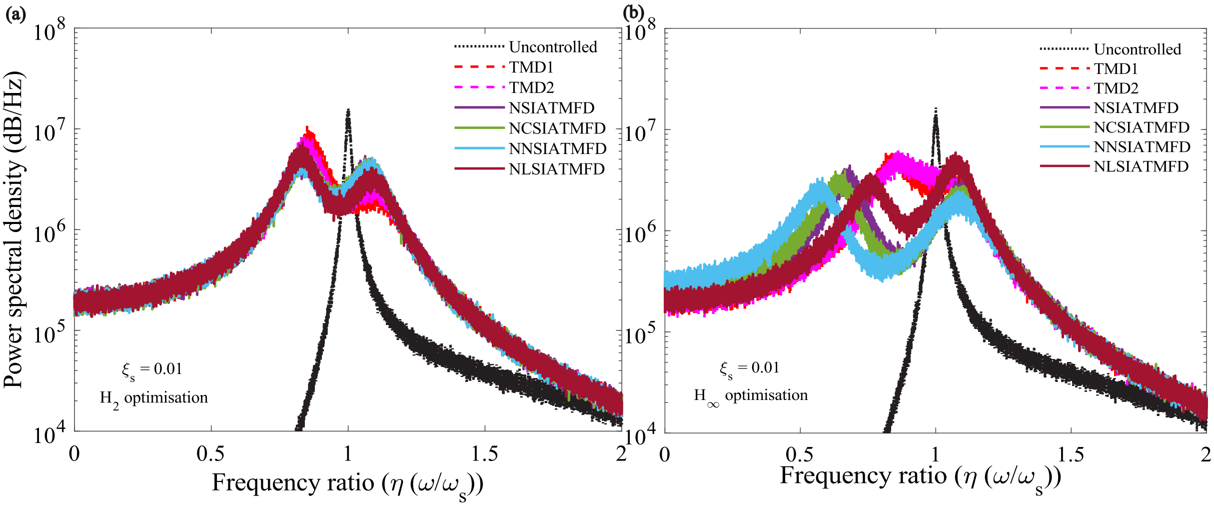

Fig. 9. The dynamic responses of the main structure are controlled by the (a) H_2 and (b) H_∞ optimised dampers subjected to random excitation.

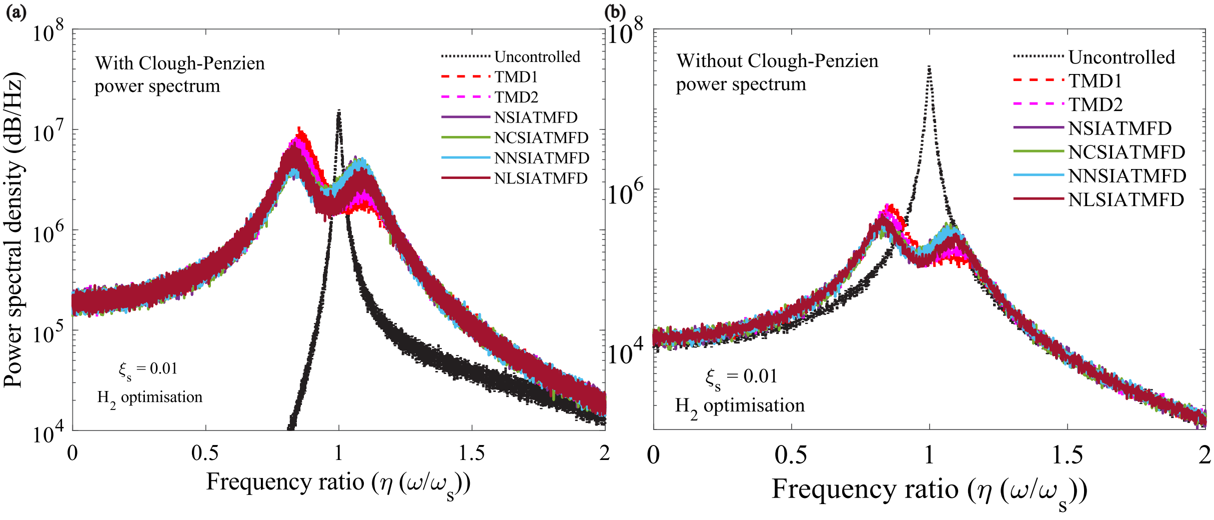

Fig. 10. The dynamic responses of the main structures are controlled by the dampers subjected to (a) with and (b) without Clough–Penzien power spectrum for random excitations.

Table 6
The near-field earthquake records.

Earthquake	Year	M_w	Recording station	Vs_{30} (m/s)	Component	E_s (km)	PGA,g
Irpinia, Italy-01	1980	6.9	Sturno	1000	MUL009	30.4	0.31
Superstition Hills-02	1987	6.5	Parachute Test Site	349	SUPERST	16.0	0.42
Loma Prieta	1989	6.9	LOMAP	371	HEC000	27.2	0.38
Erzican, Turkey	1992	6.7	Erzincan 11	275	ERZIKAN	9.0	0.49
Cape Mendocino	1992	7.0	CAPEMEND	713	NIS090	4.5	0.63
Landers	1992	7.3	Lucerne	685	LANDERS	44.0	0.79
Northridge-01	1994	6.7	Rinaldi Receiving Sta	282	NORTHR	10.9	0.87
Kocaeli, Turkey	1999	7.5	Izmit	811	KOCAELI	5.3	0.22
Chi-Chi, Taiwan	1999	7.6	TCU065	306	CHICHI	26.7	0.82
Chi-Chi, Taiwan	1999	7.6	TCU102	714	CHICHI	45.6	0.29
Duzce, Turkey	1999	7.1	Duzce	276	DUZCE	1.6	0.52

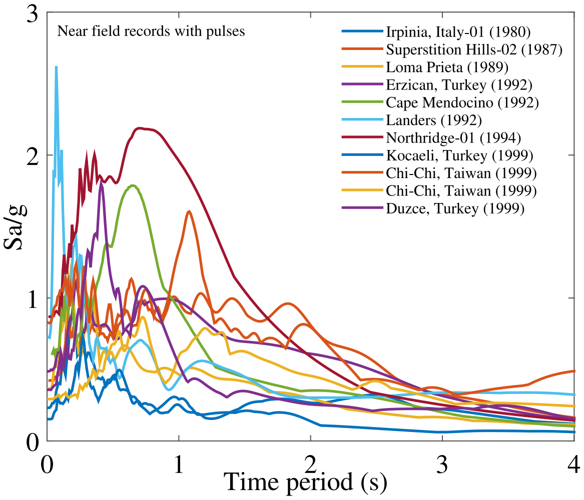

Fig. 11. The response spectra of near-field earthquake records.

simplified random input. The Clough–Penzien power spectrum significantly affects the vibration mitigation capacity by simulating realistic seismic conditions. The inclusion of this spectrum demonstrates the dampers' robustness and adaptability to real-world scenarios, highlighting their superior performance in attenuating vibrations under complex seismic loads.

3.2. Time history results

The real earthquake ground motions are considered to validate the performed methodology across a broader range of actual seismic excitation scenarios. The primary structure has a mass of 3000 tons, represented as $m_s = 3000$ tons. The structure's time period is specified as 0.5 s, represented as $T_s = 0.5$ seconds. The calculation of the structure's natural frequency relies on its time period, represented as $\omega_s = 2\pi/T_s$. The viscous damping ratio of the fundamental structure is assumed to be 0.01, represented as $\xi_s = 0.01$. The near-field earthquake record with pulses is selected from PEER Database [30] and the details are listed in Table 6. Near-field earthquakes with pulses provide a greater danger to buildings than far-field earthquakes. Consequently, the numerical analysis intended to assess the vibration attenuation efficacy of each damper utilises near-field earthquake recordings characterised by pulses with a prominent vertical component. The near-field earthquake records with pulses spectra are shown in Fig. 11 and the damping factor is considered 5%. The displacement responses of the main structures are controlled by the NSIATMFD, NCSIATMFD, NNSIATMFD, and NLSIATMFD subjected to Northridge earthquake have been obtained and shown in Fig. 12(a), Fig. 12(b), Fig. 12(c), and Fig. 12(d). According to these figures, the maximum displacements of the uncontrolled structures are evaluated as 0.0143 m. The maximum displacement of the structures controlled by the TMD is evaluated as 0.0141 m. The maximum displacements of the main structures controlled by the NSIATMFD, NCSIATMFD, NNSIATMFD, and NLSIATMFD have been evaluated as 0.0134 m, 0.0134 m, 0.0135 m, and 0.0134 m. After comparing the results of conventional and novel damper's controlled structures, it has been found that the novel dampers are 4.96% superior to the conventional dampers in terms of vibration reduction capacity. Similarly, the displacement responses are also evaluated for other considered earthquakes and listed in Table 7.

The average maximum displacement amplitude of structures controlled by the conventional and novel dampers are compared from Table 7 and substituted in Eq. (41) to obtain the displacement response reduction capacity of each novel damper.

$$D_{v_s}(\%) = \left(\frac{\left(v_s^{max}\right)^{CD} - \left(v_s^{max}\right)^{ND}}{\left(v_s^{max}\right)^{CD}} \right) \times 100 \tag{41}$$

where $\left(v_s^{max}\right)^{CD}$ and $\left(v_s^{max}\right)^{ND}$ define the maximum displacements of the structures controlled by the conventional and novel dampers. After the substitution, it has been found that the NSIATMFD, NCSIATMFD, NNSIATMFD, and NLSIATMFD have 15.30%, 15.16%, 15.59%, and 15.59% more displacement reduction capacity than the conventional dampers. The acceleration responses of the main structures are controlled by the NSIATMFD, NCSIATMFD, NNSIATMFD, and NLSIATMFD subjected to Northridge earthquake have been obtained and shown in Fig. 13(a), Fig. 13(b), Fig. 13(c), and Fig. 13(d). According to these figures, the maximum accelerations of the uncontrolled structures are evaluated as 2.3913 $\mathrm{m/s^2}$. The maximum displacement of the structures controlled by the TMD is evaluated as 1.6662 $\mathrm{m/s^2}$. The maximum displacements of the main structures controlled by the NSIATMFD, NCSIATMFD, NNSIATMFD, and NLSIATMFD have been evaluated as 1.2623 $\mathrm{m/s^2}$, 1.2555 $\mathrm{m/s^2}$, 1.2675 $\mathrm{m/s^2}$, and 1.2573 $\mathrm{m/s^2}$. After comparing the results of conventional and novel damper's controlled structures, it has been found that the novel dampers are 24.24%, 24.64%, 23.92%, and 24.54% superior to the conventional dampers in terms of vibration reduction capacity. The average maximum acceleration amplitude of structures controlled by the conventional and novel dampers are compared from Table 8 and substituted in Eq. (42) to obtain the acceleration response reduction capacity of each novel damper.

$$A_{\ddot{v}_s}(\%) = \left(\frac{\left(\ddot{v}_s^{max}\right)^{CD} - \left(\ddot{v}_s^{max}\right)^{ND}}{\left(\ddot{v}_s^{max}\right)^{CD}} \right) \times 100 \tag{42}$$

where $\left(\ddot{v}_s^{max}\right)^{CD}$ and $\left(\ddot{v}_s^{max}\right)^{ND}$ define the maximum accelerations of the structures controlled by the conventional and novel dampers. After the substitution, it has been found that the NSIATMFD, NCSIATMFD, NNSIATMFD, and NLSIATMFD have 17.61%, 17.49%, 17.70%, and 17.52% more acceleration reduction capacity than the conventional dampers.

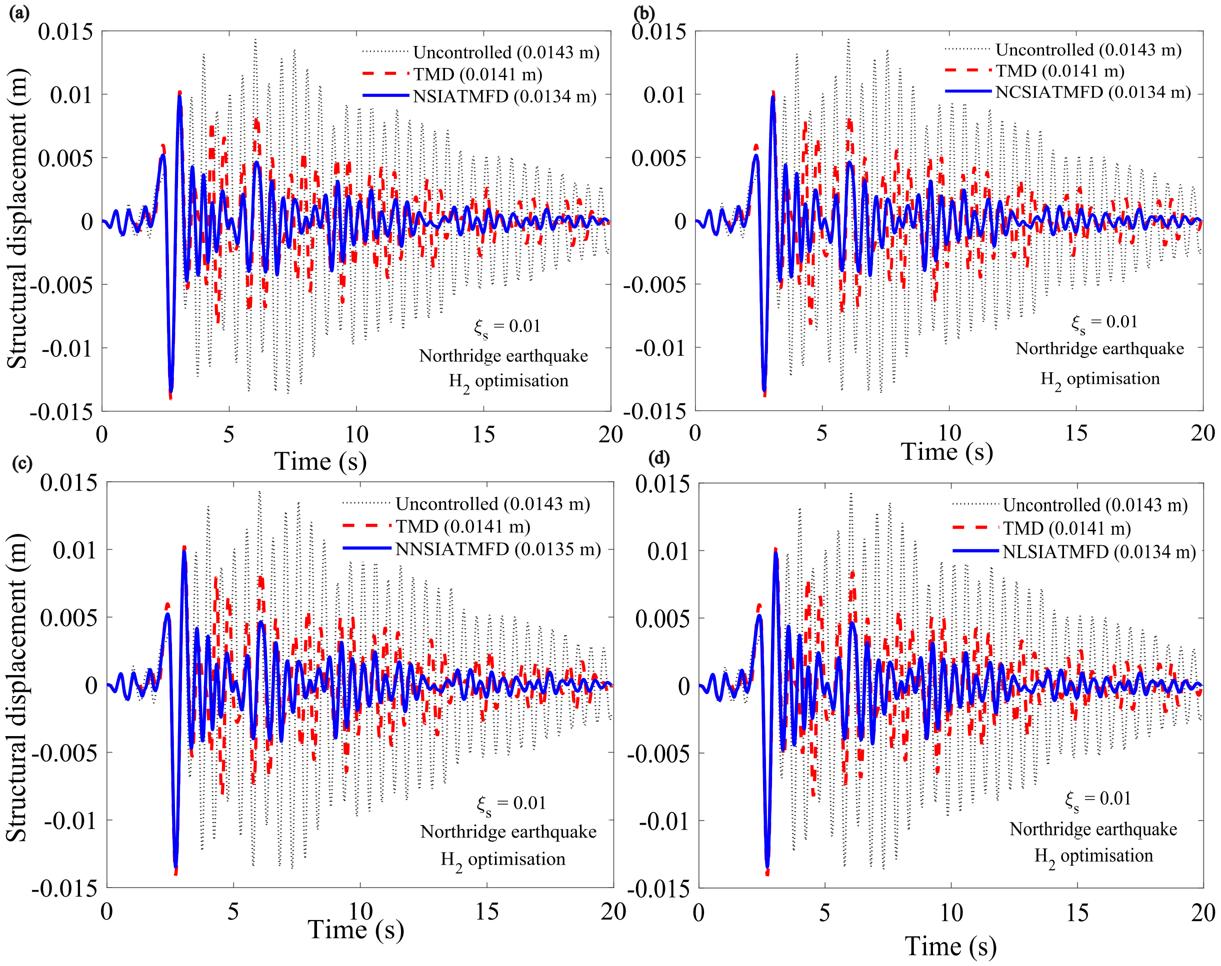

Fig. 12. The displacement responses of the main structures are controlled by the (a) NSIATMFD, (b) NCSIATMFD, (c) NNSIATMFD, and (d) NLSIATMFD subjected to Northridge earthquake. .

Table 7
The maximum displacement responses of the uncontrolled structure and structures controlled by conventional, novel dampers.

Earthquake	v_s^{max} (m)					
	Uncontrolled	TMD	NSIATMFD	NCSIATMFD	NNSIATMFD	NLSIATMFD
Irpinia, Italy-01	0.0059	0.0051	0.0043	0.0043	0.0042	0.0043
Superstition Hills-02	0.0082	0.0055	0.0040	0.0041	0.0040	0.0041
Loma Prieta	0.0055	0.0040	0.0034	0.0034	0.0034	0.0034
Erzican, Turkey	0.0066	0.0064	0.0055	0.0055	0.0054	0.0055
Cape Mendocino	0.0117	0.0082	0.0080	0.0080	0.0080	0.0080
Landers	0.0041	0.0035	0.0024	0.0024	0.0024	0.0024
Northridge-01	0.0143	0.0141	0.0135	0.0134	0.0135	0.0134
Kocaeli, Turkey	0.0044	0.0039	0.0023	0.0024	0.0023	0.0024
Chi-Chi, Taiwan	0.0088	0.0069	0.0051	0.0051	0.0050	0.0051
Chi-Chi, Taiwan	0.0063	0.0051	0.0043	0.0043	0.0043	0.0043
Duzce, Turkey	0.0110	0.0072	0.0064	0.0064	0.0065	0.0064
Average	0.007891	0.006355	0.005382	0.005391	0.005364	0.005391

4. Summary and conclusions

This paper introduces innovative nonlinear stiffened inertial amplifier tuned mass friction dampers (NSIATMFDs) and their three advanced variants: nonlinear compound (NCSIATMFD), nested (NNSIATMFD), and levered (NLSIATMFD) designs. These novel dampers integrate stiffness and mass amplification mechanisms to overcome the limitations of conventional tuned mass dampers (TMDs) in terms of narrow frequency bandwidth and limited adaptability. Through H_2 and H_∞ optimisation strategies, exact closed-form solutions for the optimal parameters of these dampers were derived. Frequency domain responses under harmonic and random noise excitations, validated using the Newmark-beta method, demonstrated significant improvements in vibration mitigation capabilities. Comparative analyses using near-field earthquake records further highlighted their effectiveness in reducing structural responses. The proposed designs consistently outperformed conventional TMDs in terms of vibration reduction capacity, with improvements of up to 24.54% under seismic excitations.

Key contributions of this research include:

- Integration of stiffness amplification elements for extended frequency control.

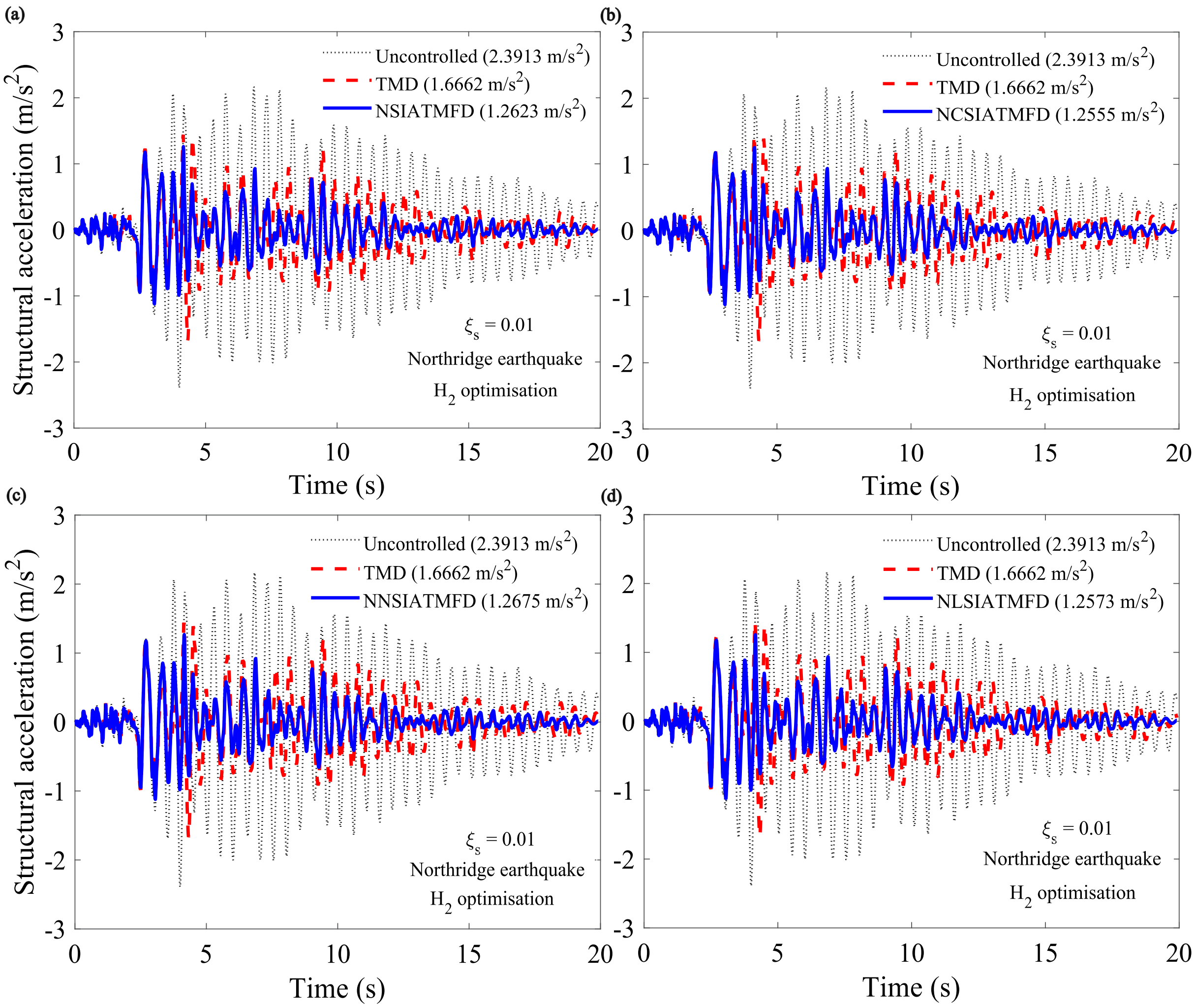

Fig. 13. The acceleration responses of the main structures are controlled by the (a) NSIATMFD, (b) NCSIATMFD, (c) NNSIATMFD, and (d) NLSIATMFD subjected to Northridge earthquake.

Table 8
The maximum acceleration responses of the uncontrolled structure and structures controlled by conventional, novel dampers.

Earthquake	$\ddot{v}_s^{max}$ (m/s^2)					
	Uncontrolled	TMD	NSIATMFD	NCSIATMFD	NNSIATMFD	NLSIATMFD
Irpinia, Italy-01	0.7932	0.4229	0.4159	0.4180	0.4144	0.4174
Superstition Hills-02	1.1648	1.0516	0.7295	0.7321	0.7273	0.7315
Loma Prieta	0.8531	0.7244	0.6050	0.6053	0.6049	0.6052
Erzican, Turkey	0.9524	0.7843	0.7653	0.7663	0.7645	0.7661
Cape Mendocino	1.6169	1.5511	1.4517	1.4532	1.4506	1.4528
Landers	1.2678	1.0256	0.8429	0.8463	0.8404	0.8454
Northridge-01	2.3913	1.6662	1.2623	1.2555	1.2675	1.2573
Kocaeli, Turkey	0.7072	0.6311	0.4008	0.4012	0.4002	0.4011
Chi-Chi, Taiwan	1.3977	0.8792	0.6945	0.6994	0.6909	0.6981
Chi-Chi, Taiwan	0.8644	0.5646	0.4984	0.5020	0.4958	0.5011
Duzce, Turkey	1.8135	1.0309	0.8457	0.8449	0.8463	0.8451
Average	1.256573	0.939264	0.773818	0.774927	0.772982	0.774645

- Enhanced energy dissipation through frictional damping mechanisms.
- Robust performance across diverse dynamic conditions, including seismic applications.

These findings establish the proposed dampers as a promising solution for modern engineering challenges, offering efficient and adaptive vibration control for structures subjected to broadband and unpredictable excitations. Future work may explore applications to multi-degree-of-freedom systems to expand their applicability further.

CRediT authorship contribution statement

Sudip Chowdhury: Writing – review & editing, Writing – original draft, Visualization, Validation, Supervision, Software, Resources, Project administration, Methodology, Investigation, Funding acquisition, Formal analysis, Data curation, Conceptualization. **Sondipon Adhikari:** Writing – review & editing, Supervision, Software, Resources, Project administration, Methodology, Investigation, Conceptualization.

Declaration of competing interest

The authors declare that they have no known competing financial interests or personal relationships that could have appeared to influence the work reported in this paper.

Acknowledgements

The authors would like to acknowledge the Post Doctoral grant received from The University of Glasgow during the period of this research work.

Appendix. The closed-form expressions of Z_1, Z_2, and Z_3 from Eq. (39)

The closed-form expressions of Z_1, Z_2, and Z_3 from Eq. (39) are listed below.

$$Z_1 = -32\eta_d^4\eta_{1,2}^4\left(\mu\gamma_m+1\right)^4\left(\mu\gamma_d\gamma_m+\gamma_d+1\right)^3\left(\mu\eta_{1,2}^2\gamma_d\gamma_m+\eta_{1,2}^2\gamma_d+\eta_{1,2}^2-1\right). \tag{A.1}$$

$$Z_2 = \begin{array}{c} -16\eta_d^2\left(\begin{array}{c} \eta_{1,2}^2\,\eta_d^4\left(\kappa\gamma_k+1\right)^2\left(\mu\gamma_m+1\right)^4\gamma_d^4 \\ -2\eta_d^2\left(\left(-2\kappa\gamma_k-2\right)\eta_d^2+\left(\mu\gamma_m+1\right)\eta_{1,2}^2\right) \\ \left(\eta_{1,2}^2-\frac{1}{4}\right)\left(\mu\gamma_m+1\right)^3\left(\kappa\gamma_k+1\right)\gamma_d^3 \\ \left(\mu\gamma_m+1\right)^2\left(\eta_{1,2}^2-\frac{1}{2}\right) \\ +\left(\begin{array}{c} 6\left(\kappa\gamma_k+1\right)^2\eta_d^4 \\ -6\eta_{1,2}^2\left(\kappa\gamma_k+1\right)\left(\mu\gamma_m+1\right)\eta_d^2 \\ +\left(\mu\gamma_m+1\right)^2\left(\eta_{1,2}^2-\frac{1}{2}\right)\eta_{1,2}^2 \end{array}\right)\gamma_d^2 \\ +2\left(\begin{array}{c} 2\left(\eta_{1,2}^2-\frac{3}{4}\right)\left(\kappa\gamma_k+1\right)^2\eta_d^4 \\ -3\left(\eta_{1,2}^2-\frac{3}{4}\right)\left(\mu\gamma_m+1\right)\left(\kappa\gamma_k+1\right)\eta_{1,2}^2\,\eta_d^2 \\ +\left(\mu\gamma_m+1\right)^2\left(\eta_{1,2}^2-\frac{1}{2}\right)^2\eta_{1,2}^2 \end{array}\right) \\ \left(\mu\gamma_m+1\right)\gamma_d \\ +\left(\eta_{1,2}^2-1\right)\left(\left(-\kappa\gamma_k-1\right)\eta_d^2+\left(\mu\gamma_m+1\right)\eta_{1,2}^2\right)^2 \end{array}\right) \\ \left(\mu\gamma_m+1\right)^2\eta_{1,2}^2 \end{array}. \tag{A.2}$$

$$Z_3 = \begin{array}{c} -2\left(-\left(\kappa\gamma_k+1\right)\left(1+\left(\mu\gamma_m+1\right)\gamma_d\right)\eta_d^2+\left(\mu\gamma_m+1\right)\eta_{1,2}^2\right) \\ \left(-\left(\kappa\gamma_k+1\right)\left(\left(\mu\gamma_m+1\right)\eta_{1,2}^2\gamma_d+\eta_{1,2}^2-1\right)\eta_d^2+\eta_{1,2}^2\left(\mu\gamma_m+1\right)\left(\eta_{1,2}^2-1\right)\right) \\ \left(\begin{array}{c} \left(\kappa\gamma_k+1\right)^2\left(1+\left(\mu\gamma_m+1\right)\gamma_d\right)^2\eta_d^4+\left(\mu\gamma_m+1\right)^2\eta_{1,2}^4 \\ -2\left(\kappa\gamma_k+1\right)\left(\left(\mu\gamma_m+1\right)\left(\eta_{1,2}^2-\frac{1}{2}\right)\gamma_d+\eta_{1,2}^2\right)\left(\mu\gamma_m+1\right)\eta_d^2 \end{array}\right) \end{array}. \tag{A.3}$$

Data availability

No data was used for the research described in the article.

References

[1] Araz O, Kahya V. Design of series tuned mass dampers for seismic control of structures using simulated annealing algorithm. Arch Appl Mech 2021;91(10):4343–59.

[2] Kaynia AM, Veneziano D, Biggs JM. Seismic effectiveness of tuned mass dampers. J Struct Div 1981;107(8):1465–84.

[3] Yang F, Sedaghati R, Esmailzadeh E. Vibration suppression of structures using tuned mass damper technology: A state-of-the-art review. J Vib Control 2022;28(7–8):812–36.

[4] Richiedei D, Tamellin I, Trevisani A. Beyond the tuned mass damper: a comparative study of passive approaches to vibration absorption through antiresonance assignment. Arch Comput Methods Eng 2022;29(1):519–44.

[5] Li Q, Zhi L-H, Tuan AY, Kao C-S, Su S-C, Wu C-F. Dynamic behavior of Taipei 101 tower: Field measurement and numerical analysis. J Struct Eng 2011;137(1):143–55.

[6] Huo Z, Ding H, Shu Z. Optimal design of tuned inerter eddy current damper. Soil Dyn Earthq Eng 2023;171:107942.

[7] Chowdhury S, Adhikari S. Nonlinear inertial amplifier liquid column dampers. Appl Math Model 2024;115875.

[8] Roberts JB, Spanos PD. Random vibration and statistical linearization. Courier Corporation; 2003.

[9] Den Hartog J. Mechanical Vibrations. New York: McGraw-Hill Book Company, Inc.; 1956.

[10] Chowdhury S, Banerjee A, Adhikari S. From impact to control: Inertially amplified friction bearings. ASCE- ASME J Risk Uncertain Eng Syst A: Civ Eng 2024;10(4):04024071.

[11] Yilmaz C, Hulbert GM, Kikuchi N. Phononic band gaps induced by inertial amplification in periodic media. Phys Rev B— Condens Matter Mater Phys 2007;76(5):054309.

[12] Adhikari S, Banerjee A. Enhanced low-frequency vibration energy harvesting with inertial amplifiers. J Intell Mater Syst Struct 2022;33(6):822–38.

[13] Settimi V, Lepidi M, Bacigalupo A. Analytical spectral design of mechanical metamaterials with inertia amplification. Eng Struct 2023;274:115054.

[14] Chowdhury S, Banerjee A, Adhikari S. The optimal design of dynamic systems with negative stiffness inertial amplifier tuned mass dampers. Appl Math Model 2023;114:694–721.

[15] Cheng Z, Palermo A, Shi Z, Marzani A. Enhanced tuned mass damper using an inertial amplification mechanism. J Sound Vib 2020;475:115267.

[16] Zhao C, Zhang K, Zhao P, Hong F, Deng Z. Bandgap merging and backward wave propagation in inertial amplification metamaterials. Int J Mech Sci 2023;250:108319.

[17] Mu D, Wang K, Shu H, Lu J. A two-stage inertial amplification tuned mass damper with grounded stiffness element. Mech Adv Mater Struct 2023;30(19):3885–96.

[18] Gao H, Zhu J, Qu Y, Meng G. Inertia modulated meta-structure with time-varying inertia amplification. J Appl Mech 2024;91(2).

[19] Zhang Z, Zhang J, Wang L, Qian H, Wang Q, Sheng P. A novel lever-based-inerter-enhanced self-centering damping system to retrofit double-column bridge bent. Soil Dyn Earthq Eng 2021;151:107003.

[20] He H, You C, Tan P, Xiang Y, Yang K. Effective damping ratio enhancement effect of tuned inerter dampers for seismic response control of civil structures. Eng Struct 2023;279:115504.

[21] Zhao Z, Chen Q, Zhang R, Pan C, Jiang Y. Energy dissipation mechanism of inerter systems. Int J Mech Sci 2020;184:105845.

[22] Chowdhury S, Banerjee A, Adhikari S. Optimal negative stiffness inertial-amplifier-base-isolators: exact closed-form expressions. Int J Mech Sci 2022;218:107044.

[23] Warburton GB. Optimum absorber parameters for various combinations of response and excitation parameters. Earthq Eng Struct Dyn 1982;10(3):381–401.

[24] Zilletti M, Elliott SJ, Rustighi E. Optimisation of dynamic vibration absorbers to minimise kinetic energy and maximise internal power dissipation. J Sound Vib 2012;331(18):4093–100.

[25] Iwata Y. On the construction of the dynamic vibration absorbers. Jpn Soc Mech Eng 1982;820(8):150–2.

[26] Ormondroyd J, Den Hartog J. The theory of the dynamic vibration absorber. J Fluids Eng 1928;49(2).

[27] Nishihara O, Asami T. Closed-form solutions to the exact optimizations of dynamic vibration absorbers (minimizations of the maximum amplitude magnification factors). J Vib Acoust 2002;124(4):576–82.

[28] Krenk S. Frequency analysis of the tuned mass damper. 2005.

[29] Kiureghian AD, Neuenhofer A. Response spectrum method for multi-support seismic excitations. Earthq Eng Struct Dyn 1992;21(8):713–40.

[30] PEER Ground Motion Database. Near-field pulse-like earthquake records. 2021, Available from the PEER Ground Motion Database at https://peer.berkeley.edu/peer-strong-ground-motion-databases.